Observations of the Bottom Boundary Layer in the Deep Western Boundary Current

by Jane Verrall

Technical Report
APL-UW TR 9404
April 1994

Applied Physics Laboratory University of Washington
1013 NE 40th Street Seattle, Washington 98105-6698

Report Documentation Page

Form Approved
OMB No. 0704-0188

1. REPORT DATE	2. REPORT TYPE	3. DATES COVERED
01 APR 1994	**N/A**	**-**

4. TITLE AND SUBTITLE	5a. CONTRACT NUMBER
Observations of the bottom boundary layer in the deep western boundary current	5b. GRANT NUMBER **NSF-OCE-9000143**
	5c. PROGRAM ELEMENT NUMBER
6. AUTHOR(S) **Jane Verrall**	5d. PROJECT NUMBER
	5e. TASK NUMBER
	5f. WORK UNIT NUMBER
7. PERFORMING ORGANIZATION NAME(S) AND ADDRESS(ES) **Applied Physics Laboratory University of Washington 1013 NE 40th St. Seattle, WA. 98105-6698**	8. PERFORMING ORGANIZATION REPORT NUMBER **APL-UW-TR-9404**
9. SPONSORING/MONITORING AGENCY NAME(S) AND ADDRESS(ES)	10. SPONSOR/MONITOR'S ACRONYM(S)
	11. SPONSOR/MONITOR'S REPORT NUMBER(S)

12. DISTRIBUTION/AVAILABILITY STATEMENT
Approved for public release, distribution unlimited

13. SUPPLEMENTARY NOTES
Master's thesis

14. ABSTRACT
This thesis is organized into a survey of the scientific motivation for this research (Chapter 2), a description of the experiment itself and the instruments used (Chapter 3), the analysis of the data collected at sea (Chapter 4), and conclusions (Chapter 5).

15. SUBJECT TERMS

16. SECURITY CLASSIFICATION OF:			17. LIMITATION OF ABSTRACT	18. NUMBER OF PAGES	19a. NAME OF RESPONSIBLE PERSON
a. REPORT	b. ABSTRACT	c. THIS PAGE			
unclassified	**unclassified**	**unclassified**	**SAR**	**84**	

Observations of the Bottom Boundary Layer in the Deep Western Boundary Current

by

Jane Verrall

A thesis submitted in partial fulfillment
of the requirements for the degree of

Master of Science

University of Washington

1994

Approved by Thomas B. Sanford
(Chair of the Supervisory Committee)

Program Authorized
to Offer Degree School of Oceanography

Date 15 March 1994

FOREWORD

This thesis was submitted in partial fulfillment of the requirements for the degree of Master of Science in Oceanography at the School of Oceanography, College of Ocean and Fishery Sciences, at the University of Washington. Dr. Thomas B. Sanford, Principal Oceanographer at the Applied Physics Laboratory and Professor in the Department of Oceanography, was chairman of the thesis supervisory committee. Financial support for this research was provided by the National Science Foundation under Grant OCE-9000143 and by a scholarship from the Natural Science and Engineering Research Council of Canada.

Master's Thesis

In presenting this thesis in partial fulfillment of the requirements for a Master's degree at the University of Washington, I agree that the Library shall make its copies freely available for inspection. I further agree that extensive copying of this dissertation is allowable only for scholarly purposes, consistent with "fair use" as prescribed in the U.S. Copyright Law. Any other reproduction for any purposes or by any means shall not be allowed without my written permission.

Signature Jane Verrall

Date March 15, 1994

Table of Contents

List of Figures

List of Tables

Acknowledgments

This thesis could not have been completed without the steady support of my advisor Tom Sanford and my friend Dicky Allison. They both taught me more than they will ever realize. I thank them and the rest of the EM group (John Dunlap, Bob Drever, Jim Carlson and Art Bartlett) for their heroic efforts in making possible the experiment on which this thesis is based.

I thank Eric D'Asaro, Steve Riser and Richard Gammon for their willingness to be on my committee and for their insight and enthusiasm.

I also gratefully acknowledge the support and encouragement of all my dear friends in the Oceanography Department, including Eric Kunze, Joanna Muench, Dan Codiga, Holly Fair and Laura Landrum, as well as Pat Caver and Peter Kaczkowski, and many others. Mark Prater tirelessly answered my early and numerous questions; he will always be my model of gentleness and generosity. Eric Kunze provided the catalyst for this thesis by suggesting the Blake-Bahamas Outer Ridge as a site for the study of the Deep Western Boundary Current.

Chapter 1. Introduction

The atmospheric climate is thought to be strongly coupled to the thermohaline "conveyer belt" because of the large meridional and air-sea heat fluxes in the North Atlantic ocean. In addition, the deep water formation in the North Atlantic opens an enormous abyssal reservoir to atmospheric gases. The rate at which greenhouse gases are taken up by the deep ocean depends upon the volume transport of the thermohaline circulation. The thermohaline circulation is in turn driven by the atmosphere through winds, evaporation/precipitation, etc., and may, therefore, be useful as a climate indicator. Observations of the thermohaline circulation are necessary if the complex relationship between the ocean and atmospheric climate is to be understood.

Despite the relative abundance of Atlantic data, we still have a very poor understanding of the physical processes of the Deep Western Boundary Current (DWBC), from formation by deep convection, to flow along the continental rise, and finally to distribution throughout the world's oceans. Knowledge of the DWBC volume tranport is uncertain; estimates of volume transport lie between 2 and 50 Sv (1 Sv = 10^6 m^3s^{-1}) with a mean of 16 Sv (Fofonoff, 1981).

At mid-latitudes, the DWBC shows relatively little seasonal variation. This is surprising since formation of deep water occurs during winter overturning events. (This seasonal formation may bias the response of the ocean to the winter climate.) However, this variability is not seen far downstream in the DWBC for two reasons. First, after formation, these dense water masses have residence times of several years in arctic basins (Swift et al., 1980); some seasonal variability is still present in the outflow from these basins. Second, mixing between the DWBC core and slower, boundary-layer flow tends to smooth long-stream variability. Evidence for such velocity smoothing is indeed borne out in velocity measurements, such as the steady current meter time series (Figure 1.1) of Mills and Rhines (1979), and in tracer measurements, as discussed by Pickart et al. (1989) and Brewer et al. (1983). On the other hand, Lazier (1988) demonstrated that the Labrador Sea component of the DWBC responded to decadal variations in climate. Brewer et al. noted rapid (on the order of a few years) response of deep water formation to climatic perturbation in the Greenland and Iceland Seas. Therefore, measurements of the DWBC are well-suited for monitoring climate change with little

sensitivity to seasonal variability.

The Florida Straits submarine cable (Larsen and Sanford, 1985) has proved to be extremely valuable and cost effective for monitoring the shallow circulation in the Atlantic. Additional monitoring sites are needed to provide accurate, long-term measurements of volume transport of the DWBC. Possible sites include overflow sills or accessible locations along the western boundary of the Atlantic. The flow at overflow sills, such as the Denmark Straits, is intermittent due to the seasonal formation of deep water; such sites would best suit process studies of deep convection. Average transport is better measured further downstream where the currents are steadier. However, a preliminary, detailed study of DWBC kinetics is required before a program to monitor the DWBC transport can begin. We performed such a study and it is the subject of this document.

Our understanding of the kinetics of the DWBC is no better than our knowledge of its volume transport. The dynamics of an intense abyssal current flowing over thousands of kilometers of sea-floor cannot be ignored. Our knowledge of this flow's force balance, energetics and internal dissipation is minimal. Transport, topographic stress, entrainment and mixing all need to be quantified. In particular, the bottom boundary layer of this current has not been well measured; this layer may be important in both the dynamics and the mixing of the deep currents. Direct observations of these physical properties of the flow are needed to improve our understanding of the kinetics of the DWBC and to constrain general circulation numerical models. An improved understanding of DWBC dynamics will provide an opportunity to start monitoring the DWBC transport.

The data described in this report were gathered during an expedition in August 1992 to survey the Deep Western Boundary Current (DWBC) in the North Atlantic ocean. We chose the Blake-Bahamas Outer Ridge (BBOR) as the site for a study of the transport and kinetics of the DWBC. There have been two surveys of the deep flow at this site: an hydrographic section by Amos et al. (1971), and a one year current meter deployment (Figure 1.1) by Mills and Rhines (1979) and tritium section (Jenkins and Rhines, 1980). Their data indicated narrow, intense currents along the northeast slope of the Ridge, with a diffuse return flow on the opposite side of the Ridge. These results are consistent with a recent Freon survey of the BBOR (Fine, personal communication.) The steadiness of the current meter records suggested the BBOR as an ideal site to

study the structure and kinetics of the DWBC.

This thesis is organized into a survey of the scientific motivation for this research (Chapter 2), a description of the experiment itself and the instruments used (Chapter 3), the analysis of the data collected at sea (Chapter 4), and conclusions (Chapter 5).

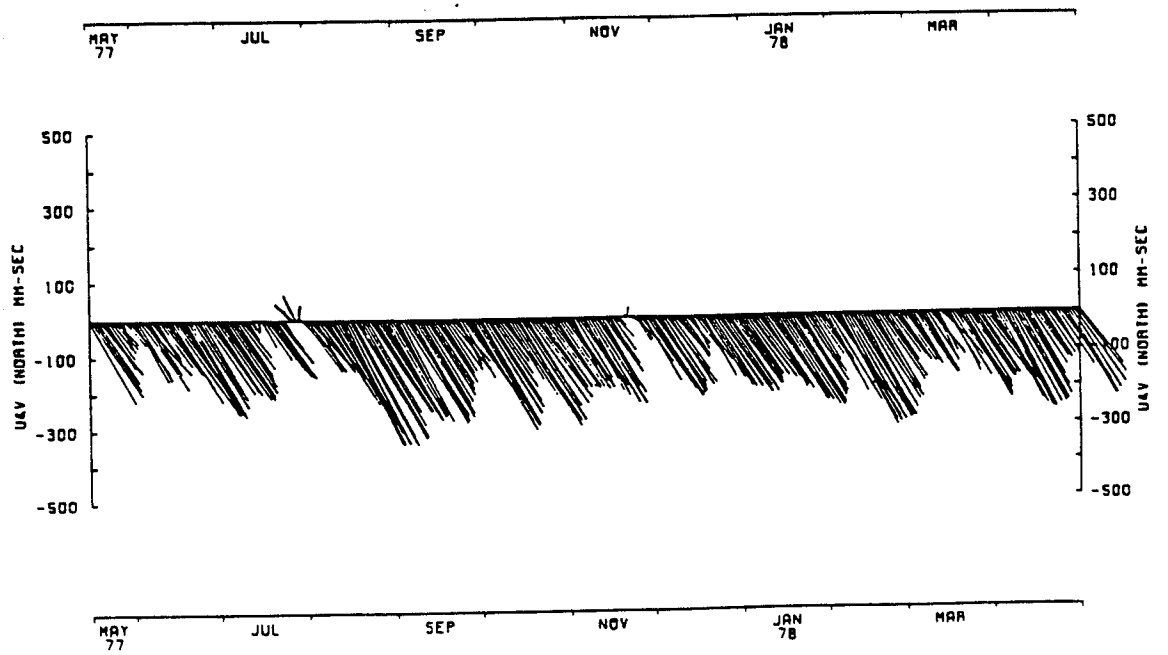

Figure 1.1. Current meter time-series in the Deep Western Boundary Current from the north-east flank of the Blake-Bahamas Outer Ridge (from Mills and Rhines, 1979). These data show strong, steady flow to the south-east, parallel to the bathymetric contours. The current meter was at a depth of 3800 m in 4000 m deep water.

Chapter 2. Scientific Background and Goals

2.1 Previous Research

Stommel (1958) postulated that the Deep Western Boundary Current (DWBC) in the Atlantic ocean was formed and driven by the sinking of dense surface water at northern latitudes. Swallow and Worthington (1961) reported the first observations of the DWBC, and since then several hydrographic surveys and current meter time series have been made which document the persistent nature of this current. We have limited our discussion to those observations of the DWBC in the vicinity of the Blake-Bahama Outer Ridge (BBOR).

Amos et al. (1971), using a salinity-temperature-depth (STD) system, observed the DWBC in a section across the BBOR. They chose a level of no motion at approximately 2000 m and estimated a volume transport of 22 Sv along the eastern flank of the Ridge and a transport of 10 Sv along the Blake Escarpment. Tracking 2000 m deep SOFAR floats along the Blake Escarpment, Riser et al. (1978) observed southward flow speeds of greater than 30 cm s^{-1} and estimated an upper bound for transport of 40 Sv. The difference in transport at the Blake Escarpment was due in part to the level of no motion at 2000 m chosen by Amos et al., the depth at which Riser et al. observed significant currents.

Mills and Rhines (1979) reported year-long current meter time series from the BBOR (Figure 1.1). These data showed strong, steady currents with deep flow parallel to the bathymetry. The deep flow on the eastern flank of the BBOR had a mean of 22 cm s^{-1} with variability of 6.5 cm s^{-1} rms. In Chapter 4, we present an analysis of these data to describe the variability of the flow and show that it was primarily due to topographic Rossby waves. The current meter mooring in the core of the current was lost, presumably due to strong currents. Mills and Rhines did not estimate the DWBC volume transport.

A tritium section (Jenkins and Rhines, 1980) across the Ridge showed a distinct core on the eastern flank, but much more diffuse concentrations to the west (Figure 2.1a). The dynamics of the flow at the tip of the Ridge were likely responsible for enhanced mixing of the DWBC with neighbouring waters. This effect might well be

responsible for the lack of integrity of the DWBC to the south of the BBOR. The tritium section of Olson et al. (1986) off the Bahamas (Figure 2.1b) showed lower concentrations and a much wider, less topographically bound core (200 km width at the Bahamas versus 20 km at the BBOR). The spreading of the core might be due to separation from topography and mixing as the DWBC rounds the tip of the BBOR. Another mechanism could be lateral mixing between the DWBC and a subtropical recirculation gyre to the east of the Bahamas. The lower concentrations might also be due to the decrease of atmospheric tritium since the measurements of Olson et al. were made four years after those of Jenkins and Rhines.

Another interesting comparison of these two tritium sections was made by Olson et al. (1986). The core of tritium at the BBOR was deeper (at 4200 m) and colder (θ = 1.9 °C) than the tritium core off the Bahamas (at 3000 m and 2.5 °C) measured four years later. To explain the 0.6 °C difference between the two cores, Olson et al. suggested a change in North Atlantic Deep Water formation to higher temperatures. Although no change greater than 0.05 °C was observed in the smoothed DWBC temperature at 36°N (Figure 2.2) between IGY (International Geophysical Year, 1957 to 1959) and 1981 by Roemmich and Wunsch (1984), it is possible that larger temperature changes occured over shorter periods. In the Labrador Sea, time series of deep temperature (Figure 2.3) showed that changes as large as 0.3 °C could occur in a few years (Lazier, 1988).

The change in depth of the tritium core is also difficult to explain. Hogg and Stommel (1985) observed that the DWBC seemed to flow at 3400 m ± 200 m from the Grand Banks of Newfoundland to Cape Hatteras, and then, after passing under the Gulf Stream, flowed at 4200 m ± 200 m at the Blake-Bahama Rise. They did not reference the sources of these data; we assume that the estimate of the DWBC depth at the BBOR was from Jenkins and Rhines (1980). Hogg and Stommel argued that the DWBC might show a tendency to maintain its thickness as it crossed under the thermocline associated with the Gulf Stream. Although this argument might explain why the DWBC should drop to 4200 m after it crossed under the Gulf Stream, why then should the tritium core reappear at 3000 m in the Olson et al. sections off the Bahamas? The recirculation gyre of the Bahamas might be responsible for the core becoming shallower.

We hypothesize instead that the depth of the DWBC core at the BBOR is shallower than 4200 m but was not well resolved by the Jenkins and Rhines (1980) tritium data because of the nature of the BBOR topography. The tritium section crossed the BBOR where the Ridge crest is at a depth of 3700 m. If the DWBC core were at a nominal depth of 3200 m and if flow near the bottom were to follow depth contours, such as the dashed arrows in Figure 2.4, the bulk of the DWBC core would cross the Ridge upstream of the Jenkins and Rhines (1980) section. In this case, it is possible that the core of high tritium water seen at the Bahamas at 3000 m is indeed present at the BBOR, but crosses the Ridge crest in waters say between 3000 and 3500 m deep. The measured current vectors in Figure 2.4 show backing of velocity consistent with shallower flow crossing the Ridge crest and deeper flow following bathymetric contours. A survey of the deep flow at the BBOR should reveal the depth of the DWBC velocity core and whether the difference in tritium cores observed by Olson et al. (1986) can be explained by depth-dependent currents tightly constrained to follow topography.

Richardson (1977) deployed six near-bottom current meters off Cape Hatteras to study the crossover between the Gulf Stream and the DWBC. The mean current meter vectors were all approximately parallel to the bathymetric contours. A silicate section along the current meter line showed that the DWBC was anomalously low in silicate. The core of the DWBC (with a silicate anomaly over 3 μg atoms l^{-1}) was located between 2500 and 4000 m depth; the center of the core was at approximately 3200 m! Unfortunately, at Richardson's section, the DWBC was directly under the Gulf Stream, so it is impossible to estimate whether the DWBC dropped to 4200 m depth after crossing under the Gulf Stream.

We have discussed research on the effect of the Gulf Stream on the DWBC, but there has also been some progress in studying the effect of the DWBC on the Gulf Stream. Thompson and Schmitz (1989) described the results of a two-layer primitive equation numerical model in which the increase in transport of the DWBC decreased the latitude at which the Gulf Stream separated from the continental boundary. Leaman (1989) observed a relationship between the strength of the DWBC and meander characteristics of the Gulf Stream; the relationship was consistent with the model results. Further observations of the DWBC south of Cape Hatteras are needed for comparing DWBC volume transport and core depth with Gulf Stream meanders determined from

satellite images.

Off Cape Hatteras, Pickart and Watts (1990) deployed current meters 200 m above the bottom (Figure 2.5a). The striking feature of their data was the presence of energetic, 40-day period, bottom-trapped topographic Rossby waves (TRWs) with speeds equal to that of the DWBC.

To the south, Lai (1984) showed 100-day current meter records (Figure 2.5b) from the Blake Escarpment, 300 km to the southwest of the BBOR. Lai estimated a mean southward transport of the deep flow to be 24 Sv. He also suggested that fluctuations in observed currents might be due to meandering of the current away from the mooring or the presence of an eddy in the mean current. In either case, this explains how first order variations might be observed in velocity even though the volume transport remains unchanged.

Further to the south, Fine and Molinari (1988) observed distinct upper and lower cores of high CCl_3F or Freon-11 (F-11) off Abaco Island, the Bahamas. The upper core (1000-1700 m) was of Labrador Sea origin and the lower core (3200-4600 m) consisted of Norwegian Sea and Denmark Straits Overflow Water. Fine (personal communication) also measured F-11 concentrations at the BBOR; these data were consistent with the hypothesis that an upper part of the deep core flows across the Ridge before reaching the Jenkins and Rhines section. Velocity surveys across the BBOR will greatly help to interpret the Freon distribution at the Ridge.

Lee et al. (1990) measured deep currents (Figure 2.5c) with current meter moorings east of Abaco at 26.5°N. They observed core speeds of 20 cm s^{-1} at 2500 m and a southward transport of 33 Sv. At least half of this transport was estimated to be due to a deep cyclonic recirculation gyre off the Bahamas. Variation in transport was dominated by 70 to 100-day time scale events that appeared to be caused by meandering of the DWBC core.

Leaman and Harris (1990) combined hydrographic sections with Pegasus velocity measurements east of Abaco. The velocity core here was offshore from the DWBC core from tracer studies, with an estimated deep transport of 35 Sv. They suggested that the offshore velocity core and high volume transport indicate either a deep recirculation gyre or the augmented DWBC flow found in some theoretical models.

Freons are particularly intriguing as tracers since they can be used to date the surface formation of water parcels in the DWBC. The ratio of F-11 (CCl_3F) to F-12 (CCl_2F_2) has changed with time in the atmosphere and, therefore, a measure of Freon ratios in the sea can be used to determine the time at which deep waters were last ventillated. If, in turn, the formation time of the water is known, then both the initial sea-surface Freon concentration and the change in concentration can be estimated. This decrease in concentration can be used to estimate the dilution of the DWBC due to the cummulative entrainment of Freon-free abyssal waters in the North Atlantic.

Freon dating was used by both Smethie and Trumbore (1984) and Weiss et al. (1985) in the DWBC. The average flow speed calculated by Weiss et al. was 1-2 cm s^{-1}, far below observed core speeds of 5-20 cm s^{-1}. Pickart et al. (1989) recognized this discrepancy and were able to explain the difference by improving the Freon dating technique with a simple model. The model involved two parts: a model of an arctic basin overflow and a model of the velocity structure of the DWBC. In the overflow model, mixing of sinking surface waters with basin waters of differing Freon concentrations caused an apparent aging of the overflow water of approximately five years. Further aging was found to occur downstream if the DWBC was modeled as a core of uniform velocity on the seafloor surrounded above and laterally by a "shoulder" region of slower flow. Pickart et al. were able to show that observed DWBC core speeds and measured ratios of F-11 to F-12 could be reconciled using reasonable estimates of shear and mixing in the current. This model did not include the bottom boundary layer (BBL) of the DWBC.

In deep water, Amos et al. (1971) found a cold isothermal bottom layer 20-170 m thick with relatively high Antarctic Bottom Water content. They tested bottom boundary layer theories in terms of their data: layer thickness, geostrophic velocities, sand waves from bottom photographs and bottom roughness. The study was unsuccessful; more recent theories show the importance of including the bottom slope. Amos et al. were hampered by a lack of direct velocity measurements in both their volume transport and bottom boundary layer efforts.

Detailed velocity profiles in the DWBC would be extremely valuable to help determine the frictional dynamics of bottom currents. We know that the DWBC persists without much change in depth, despite the fact that it lies close against the sloping

western edge of the ocean basin. Several recent papers (e.g., MacCready and Rhines (1991), Trowbridge and Lentz (1991), and Garrett, MacCready and Rhines (1993)) have put forth the theory that buoyancy forces along such a sloping boundary may greatly alter the Ekman layer dynamics there, leading to a boundary layer with extremely low drag. The theories have been borne out in computer simulations, laboratory experiments, and in oceanographic data from the continental shelf, yet it is in the deep ocean that such frictional forces would have the greatest importance. Measurements of velocity and density in the bottom boundary layer of the DWBC are needed to understand better abyssal flows and the global thermohaline circulation.

Currents along sloping boundaries are also thought to be a possible source of density mixing in the ocean (Garrett, 1990). While advective-diffusive models (Munk, 1966) predict basin-averaged vertical diffusivities of $O(1\ cm^2s^{-1})$, the actual diffusivities measured in mid-ocean (Gregg, 1987) are at least an order of magnitude smaller. Progress on boundary-mixing models has been hampered by the lack of data in the benthic boundary layer.

2.2 Outstanding Questions and Objectives

The preceding review of previous research in the vicinity of the Blake Bahamas Outer Ridge (BBOR) has identified several interesting scientific problems. The following points are important:

- The DWBC is an important part of the thermohaline circulation of Atlantic and global oceans.
- The wide range of DWBC transport estimates implies need for refinement.
- The flow experiences strong topographic control; cross Ridge flow, bottom drag and entrainment may be important here.
- What balances the bottom boundary layer (BBL) friction: changes in available potential energy?
- What maintains BBL thickness and exceptional homogeneity?
- How does the DWBC velocity structure affect "aging" of tracers? Does the BBL

play a role?

The overwhelming focus of previous work on the Deep Western Boundary Current (DWBC) in the North Atlantic has been on tracer results with few direction current observations and fewer still velocity profiles. Considering the importance of the DWBC in deep water renewal and global climate, we made an intensive survey of profiles of velocity and water properties at the Blake-Bahamas Outer Ridge. These observations are unique and provide a rich data set for the exploration of the variety of oceanographic questions identified in the previous section.

The Blake-Bahama Outer Ridge (BBOR) is an excellent location for the observation of this current, either once or on a long-term basis. While the DWBC could be observed anywhere along its lengthy path, we chose a site at which the flow is particularly strong, narrow and steady. The strong flow and abrupt topography were particularly important since we were interested in the topographic interaction and bottom boundary layer of the DWBC. While the water properties of the BBL have been observed (Amos et al., 1971; Rhines, personal communication), there have been no profiles of the velocity structure in the bottom boundary layer.

The objectives of this experiment were to measure the transport of the DWBC, to determine whether the BBOR might be a suitable site for monitoring the transport and to study the dynamics of the DWBC as it flows around the BBOR. In particular, we sought evidence for the existence of postulated slippery bottom boundary layers (MacCready and Rhines, 1991). This thesis focuses on a description of the observations of the frictional bottom boundary layer.

While this experiment was short-term (15 days), it is important to consider such a study of the DWBC as potentially the beginning of a long-term series of measurements of DWBC transport. This current is known to be of polar origin and is thought to reflect the amount of surface to deep water conversion. The DWBC is an important component of global climate and deep ocean ventillation. A program designed to monitor the DWBC transport over decades is necessary to improve our understanding of the global climate and its long-term rate of change.

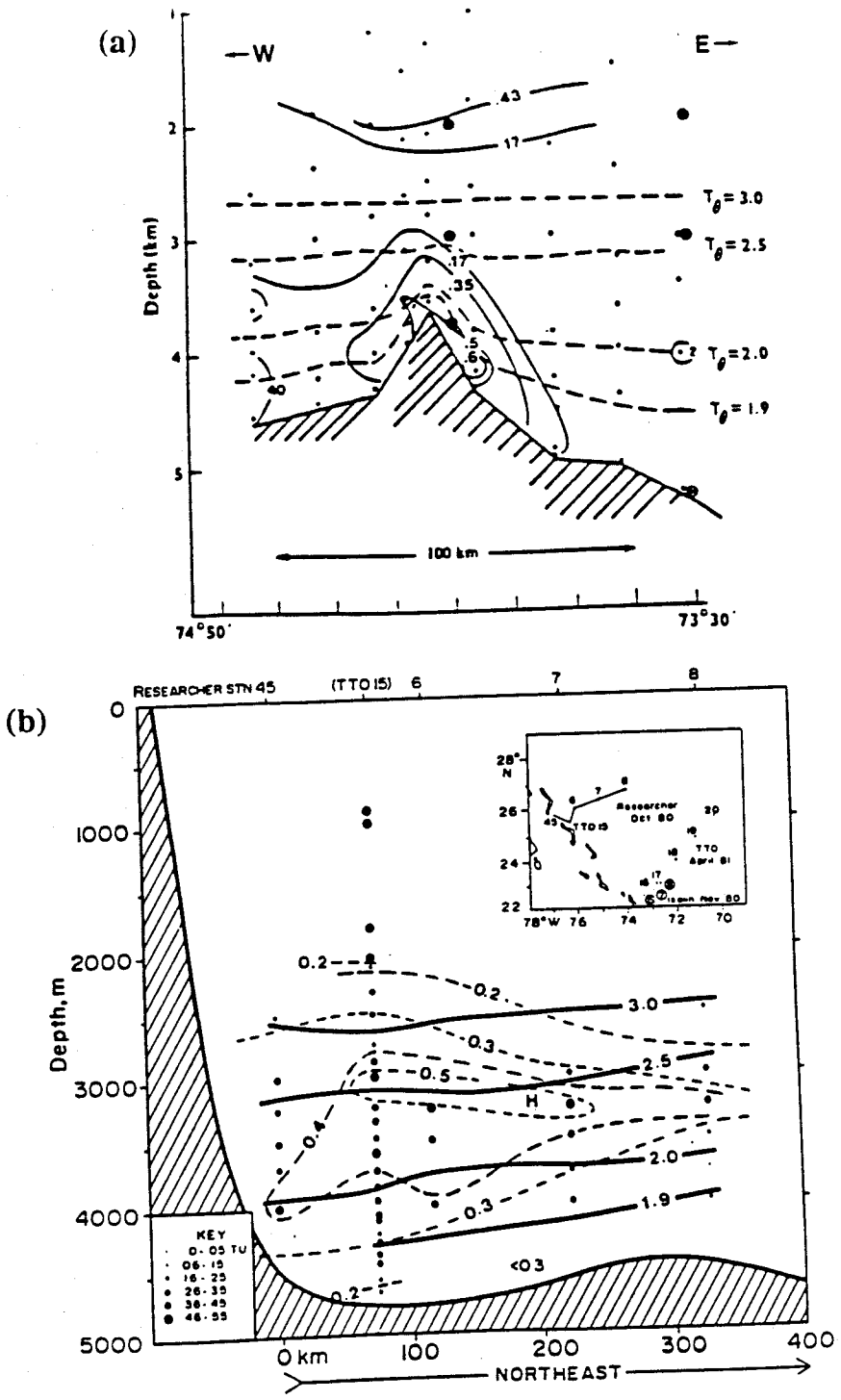

Figure 2.1. Tritium and potential temperature sections across the Deep Western Boundary Current. a) Jenkins and Rhines (1980) section across the Blake-Bahamas Outer Ridge. Contours have been changed to reflect a 1981 standard time for tritium. b) Section off the Bahamas at approximately 26.5° N (from Olson et al., 1986).

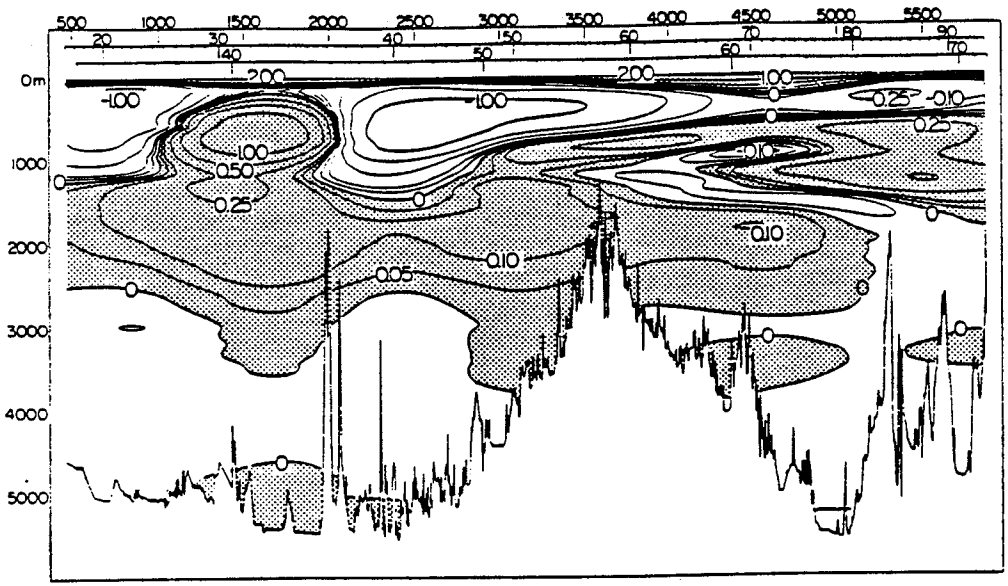

Figure 2.2. Smoothed temperature difference section at 36° N; IGY data subtracted from 1981 (from Roemmich and Wunsch, 1984).

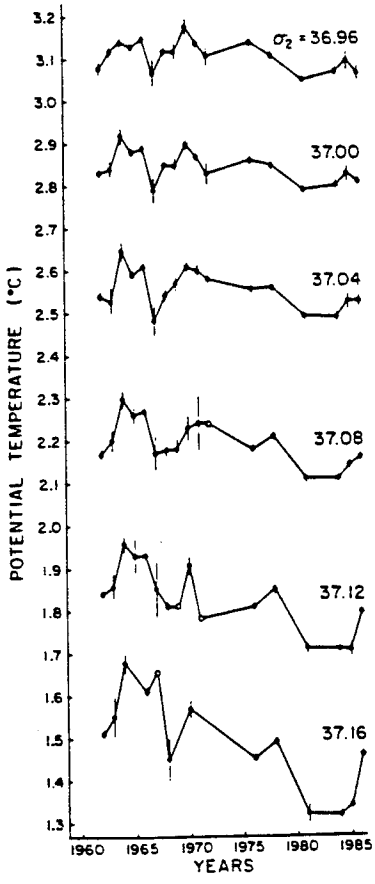

Figure 2.3. Potential temperatures on six deep and near bottom σ_2 surfaces in the western Labrador Sea (from Lazier, 1988).

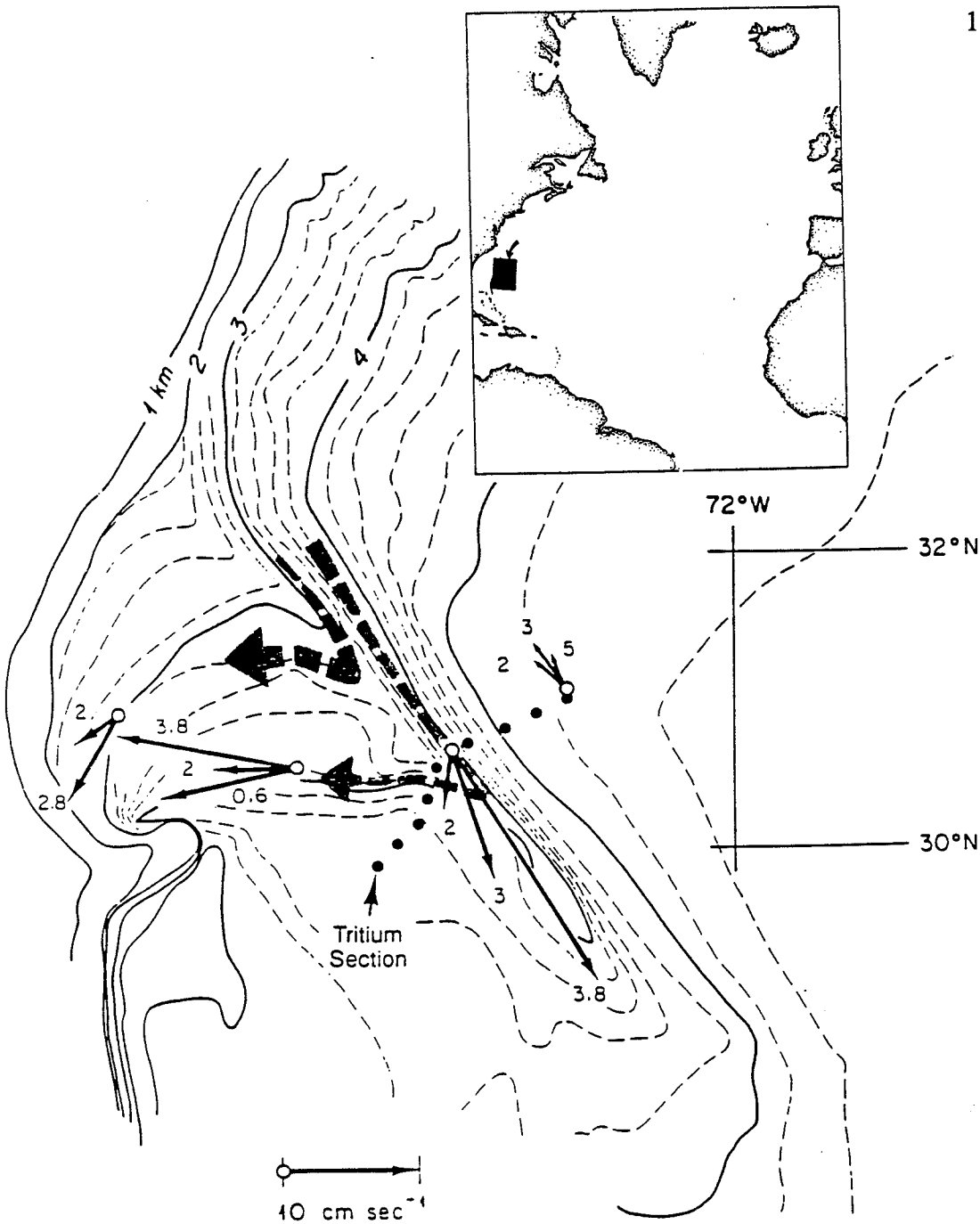

Figure 2.4. Topography and velocity observations at Blake-Bahamas Outer Ridge. Inset shows North Atlantic ocean and indicates the location of the larger chart with a black rectangle. Solid arrows represent 12-month mean currents from current meters. Depth of current meter in km is shown at arrow tip (from Jenkins and Rhines, 1980.) Dashed arrows represent hypothesized bottom flow pattern: bottom flow follows bathymetric contours. Only deep flow (at approximately 4000 m) crosses the Jenkins and Rhines tritium section.

a) Cape Hatteras (approx. 3500 m)

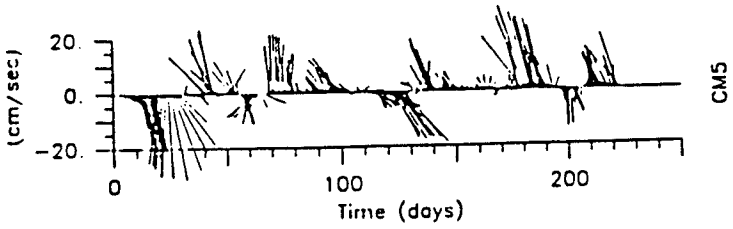

b) Blake Escarpment (4900 m)

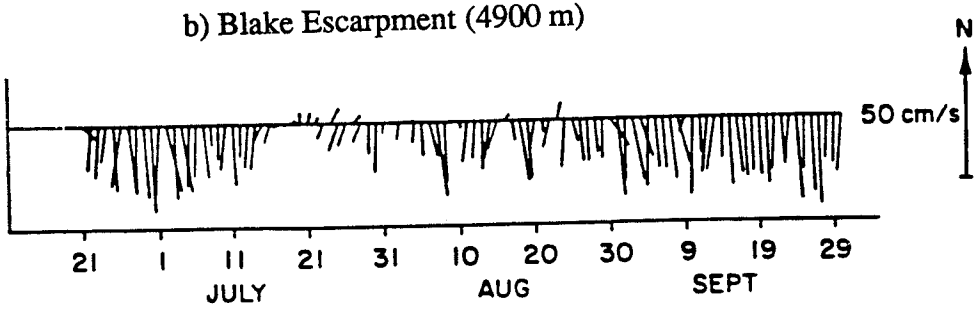

c) East of Abaco (4000 m)

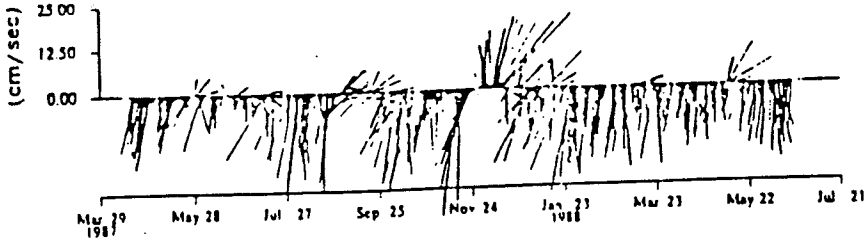

Figure 2.5. Comparison of deep current meter time series from a) Pickart and Watts (1990), b) Lai (1984), and c) Lee et al. (1990). Current meter depths are indicated in parentheses.

Chapter 3. Description of Experiment and Data

3.1 Overview of Experiment

An expedition to survey the Gulf Stream and Deep Western Boundary Current (DWBC) was made in July and August, 1992 on cruise *Endeavor* 239 (EN239). The second leg of this cruise, from July 22, 1992 to August 9, 1992, involved an intense survey of the DWBC flow around the Blake-Bahamas Outer Ridge (BBOR) at 31°N, 78°W in the North Atlantic ocean.

Profiles of velocity, temperature, conductivity and dissolved oxygen were obtained from the sea surface to the seafloor. The salinity and density of seawater were calculated from empirical relationships between the measured temperature, conductivity and pressure. In addition, the turbulent dissipation rate was measured within 2000 m of the seafloor. Finally, bottle samples for determining oxygen and nutrients were obtained using a Niskin bottle rosette and standard sea water analysis techniques.

The primary instrument used was the Absolute Velocity Profiler (AVP, Figure 3.1), a free-fall oceanographic instrument package (Sanford et al., 1985) which was redesigned and rebuilt for this experiment. The AVP had the ability to measure simultaneously the velocity and density of the deep flow; this capability was important for the success of this experiment. Standard CTD (conductivity-temperature-depth) casts were performed each night, when darkness made the recovery of the AVP more difficult.

The following sections in this chapter describe the instruments used during this experiment and the type and location of the data collected.

3.2 Instrumentation

The Absolute Velocity Profiler (AVP) has several measurement capabilities: velocity, temperature, conductivity, dissolved oxygen, and dissipation rate. Two such profilers, denoted AVP1 and AVP2, were used during this experiment. Only AVP2 was equipped with an oxygen sensor.

In general, an AVP drop consisted of a down-profile and an up-profile. The AVP was lowered over the side of the ship. A beach ball attached to the top of the AVP kept the instrument afloat so that the ship could be moved several boat lengths away before the start of the profile since the corrosion field of steel ships interferes with the electric field measurements made by the AVP. The down-profile began when the beach ball was released under command of the AVP's internal computer and ended when the lead weights suspended below the AVP hit the seafloor. The lead weights dropped off, and the AVP rose to the surface for the up-profile. At the end of the profile, the AVP floated on the surface until the ship was brought alongside it and we hooked it with a recovery line.

Velocity was measured on both the up and down traverses. Temperature and conductivity were measured by sensors on the lower end of the AVP. These data were of high quality only on the down-profile; on the up-profile the motion of the AVP stirred the water ahead of the temperature and conductivity sensors. Due to limited memory on the AVP (20 megabytes), the 400-Hz dissipation rate measurements were made only in the bottom 2000 m of the down-cast.

AVP1 completed 56 drops and AVP2 completed four during Leg 2 of EN239 at the BBOR. The locations of these profiles are discussed in Section 3.3. On AVP2's fifth drop, a leaking external connector let salt water into the instrument. The internal electronic circuitry was shorted and the batteries discharged and overheated. AVP2 was assembled and disassembled on the ship, so the orientation of the sensors in AVP2 are not known accurately. AVP1 performed well for the whole cruise, and the orientations of its sensors were carefully measured.

The AVP measures velocity in an unique way: the velocity profiles are obtained using the combined measurements of electromagnetic (EM) and acoustic Doppler instruments. The voltage measured across the instrument can be related to the velocity of the instrument. Since the AVP is a freely falling profiler, the horizontal velocity of AVP is essentially equal to that of the surrounding water. The measurement works in the following way. (For more detail on this technique, see Drever et al., 1984.) The voltage between two electrodes, in contact with sea water, is measured. This voltage can be broken up into the sum of four components. The first two of these components are due to the motion of the electrodes through the Earth's magnetic field. The two electrodes are electrically connected to a voltmeter inside the AVP. By Faraday's law,

the potential V measured by a voltmeter, attached to electrodes separated by a distance $\mathbf{l}$, moving through a magnetic field $\mathbf{B}$ at speed $\mathbf{v}$, is given by $V = \mathbf{l} \cdot \mathbf{v} \times \mathbf{B}$. The electrodes on the AVP are at the same height on the instrument, so the vector $\mathbf{l}$ is horizontal. Therefore, the first component of the voltage measured by the AVP is due to the instrument falling relative to the horizontal part of the Earth's magnetic field. Similarly, the second component of the voltage is due to the horizontal motion of the AVP through the vertical component of the Earth's magnetic field. It is this component of the voltage that yields the measure of the horizontal velocity. The third component arises from the horizontal motion of the entire water column through the Earth's magnetic field which produces an electric field which is essentially constant with depth. Finally, inhomogeneities in the electrodes themselves and thermo-saline differences in the water around the electrodes produce a potential offset between the electrodes. In summary, the AVP measures the voltage induced by the motion of AVP through the magnetic field, plus the voltage due to the electric field present in the water, plus the electrode offset.

In order to separate the voltage which is due the horizontal motion of the AVP from the other voltages, and thereby determine the desired horizontal water speed, the AVP was designed with three additional features. First, the pressure measurements are used to calculate the fall rate of the AVP, so the voltage arising from the relative vertical motion of the instrument can be determined. (We assume that the local water around the AVP is not moving vertically, so that the relative vertical motion of the AVP in the water is simply the fall rate of the instrument.) Second, to separate out the electrode offset which changes during a profile, the AVP rotates about a vertical axis: fixed turning vanes on the upper part of the AVP (Figure 3.1) cause the instrument to turn as it falls. This rotation, combined with compass measurements to determine the orientation of the instrument, is used to separate the components due to the motions of the water column and the instrument, which depend on the orientation of the instrument, from the electrode offset, which is independent of orientation. After the fall rate component and electrode offset have been removed from the data, the AVP gives a velocity profile which has a depth-independent offset induced by the water column motion through the Earth's magnetic field. This velocity offset is determined by comparing the EM velocity profile with an absolute velocity profile measured by an acoustic Doppler velocimeter. Since the 300-kHz acoustic system relies on reflecting signals off the seafloor, attenuation reduces the range of the Doppler profile to within about 300 m of the bottom; above this height, the reflected signal is too weak to determine the Doppler

shifted frequency.

The EM velocity profiles obtained from the AVP were very accurate. The two pairs of electrodes gave independent measurements of the velocity profile; for AVP1, the difference between the two profiles was typically 0.2 cm s^{-1} rms. Therefore, the noise in one profile was 0.14 cm s^{-1}. The primary source of error in the velocity profile came from the acoustic Doppler measurements. The difference in the Doppler velocity profiles between the down-casts and up-casts was 3 cm s^{-1} rms, but some of this noise could be due to instrument wobble on the up-cast.

An independent measure of the average velocity of the AVP is the difference between launch and recovery position divided by the time the AVP was in the water, A comparison of this average velocity versus the average of the velocity profiles on Leg 1 showed that the difference in average velocity was 7 cm s^{-1} rms between drops. However, there were large errors in the recovery positions, so this noise level does not reflect the accuracy of the AVP velocity measurements. The procedure for determining the recovery position was improved on Leg 2, so an analysis (not yet done) of those data should show a better comparison between the velocity averages from the two techniques.

Standard Sea-Bird Electronics, Inc. (SBE) modular temperature and conductivity sensors and Paroscientific pressure sensors were fitted to the AVP. (AVP2 also had a dissolved oxygen sensor.) Thus, the AVP provided all the functions of an accurate CTD (conductivity-temperature-depth). Temperature measurements were accurate to better than 1 m°C, and salinity measurements (derived from temperature and conductivity) were accurate to better than 0.002 PSU. The uncertainty in the pressure measurements was less than 1.5 dbar under all conditions at sea and was less than 0.75 dbar at depth.

Each AVP was fitted with two shear probes to measure the turbulent dissipation rate, which is a measure of the intensity of small scale turbulence. The dissipation measurement noise levels were typically 3×10^{-9} W kg^{-1}. In some drops, the noise floor was one to four orders of magnitude higher than this, an increase we attribute to faulty shear probes. We had anticipated quieter dissipation rate data. We think that the lead drop weights hanging below the shear probes might have intermittently shed a turbulent wake onto the shear probes. Instrument vibration might also have contributed to

the high noise. In addition, the dissipation rate data were more noisy during acoustic Doppler transmissions.

A Sea Bird 911+ CTD (conductivity-temperature-density) and Niskin bottle rosette were used to measure water properties and to provide an accurate standard with which to calibrate the temperature and conductivity sensors on the AVP. The temperature and conductivity sensors on the CTD were the same models as those on the AVP. Two sets of temperature and conductivity (T/C) sensors (a primary and secondary set) provided a redundant set of measurements and confirmation of data quality. The CTD temperature, salinity and pressure measurements had the same accuracies as the AVP measurements described above. The AVP and CTD T/C sensors were calibrated simultaneously in a common bath to improve the precision between sensors.

Both the primary and secondary temperature sensors (serial numbers 843 and 844) on the CTD were "unhealthy". Norge Larsen at SBE found that a faulty capacitor in the Model 3 temperature sensors was responsible for their abnormal behaviour. In addition, the thermistor was not properly soldered in the primary sensor; fortunately, the only problem was a slow response to temperature changes. The time constant of this sensor was 0.280 seconds compared to a nominal 0.065 seconds for a healthy sensor. This large time constant is relatively unimportant in the deep ocean where temperature changes are small over great depths, so we were able to use the primary sensor with some confidence.

A rosette with twelve 5-litre Niskin bottles was mounted above the CTD. Spring-loaded lids on the bottles snapped shut to capture water samples at desired depths. Water samples taken at various depths from the entire water column, but primarily from near the bottom, were analyzed on the ship for salinity, dissolved oxygen and nutrients (silicate, nitrate, nitrite, phosphate). Water samples were also taken back to the University of Washington for independent salinity analysis.

On five CTD profiles, the secondary CTD T/C sensors were removed and a pair of AVP sensors substituted. This provided a calibration of the AVP sensors against the CTD sensors and the water samples.

A Benthos, Inc. altimeter (an acoustic echo ranging device) was mounted on the CTD to determine the height of the CTD above the bottom. The altimeter was useful in determining the structure of the bottom boundary layer (BBL) because in studies of the

BBL, the height of observations off the bottom is more critical than the actual depth.

Two optical instruments were also mounted on the CTD to measure the amount of suspended particulate matter. One instrument was a Sea Tech Inc. transmissometer which measured the beam transmission from an LED (light emitting diode.) The second device was an optical back scatter (OBS) sensor head (OBS-3B) from D&A Instrument Company. The OBS device also had an LED transmitter; a detector adjacent to the LED determined the amount of light scattered back by particles in the water. A resistor in the sensor's front-end amplifier was changed to increase the gain so that the low concentration levels (on the order of 25 μg/l) expected in the BBOR region could be detected. The OBS sensor was also mounted on the AVP. Unfortunately, the OBS device began to function poorly (for reasons that were not understood) and caused sufficient interference in the AVP acoustic signals that it was necessary to disconnect it. Lead weights were added to the slot normally occupied by the OBS sensor so that the weight distribution of the AVP would not be adversely affected by the removal of this device. Water samples from the rosette bottles were filtered to provide an independent measure of the suspended particulate concentration. The filters were Nulceopore polycarbonate membranes with 0.4 μm diameter pore size. Static charge on the filters caused large uncertainty in the pre-cruise filter weights, and so these measurements were too uncertain to provide a useful calibration for the optical devices.

3.3 Measurement Locations

The majority of profiles were made at points along six lines, denoted Sections 0 to 5, around the BBOR (Figure 3.2). The locations of Sections 0 and 1 were planned so that the DWBC flow could be estimated before the current significantly encountered the Ridge. In particular, measurements spanning the entire DWBC at Section 0 were intended to provide an estimate of the total transport in the DWBC. The remaining sections were planned so that we could observe changes in the DWBC as it flowed along and across the Ridge. In particular, Section 2 coincided with the location of the Jenkins and Rhines (1980) tritium section. With the exception of Section 4, each section in this experiment was roughly perpendicular to the bathymetry.

A time-series station at Site 2-5 (Section 2, station 5) was planned so that temporal variability in the flow, such as tides and internal waves and topographic Rossby waves (TRWs), could be estimated. Site 2-5 coincides with the location of Mills' and Rhines' (1979) current meter mooring 618 near the Ridge crest (Figure 2.4). Ten AVP profiles and one CTD cast were made at this site. In addition, six AVP profiles on Section 2 were made about six days after the first survey of Section 2 to help resolve TRWs.

A total of 60 AVP drops and 16 CTD casts were made during this experiment. The location of the AVP drops are shown in Figure 3.3, and the location of the CTD casts in Figure 3.4. Table 3.1 lists the locations of the AVP drops and CTD casts in chronological order.

In an ordinary CTD cast, the CTD is lowered to within a few meters of the seafloor and then raised to the sea surface and returned to a secure position on the ship's deck. However, another use of the CTD is the tow-yo, which involves repeatedly lowering and raising the CTD in the water while the ship steams on a steady course. The CTD yo-yoes up and down in the water while the ship tows it; these words are combined into "tow-yo" in shipboard jargon. We made two tow-yo surveys of the bottom boundary layer: one on Section 2 (CTD 32) and one on Section 5 (CTD 39). The ship's paths for these tow-yo's are shown in Figure 3.5. The tow-yo on Section 2 curves toward the south due to strong surface currents that the ship was not able to overcome with the CTD suspended over the side J-frame. For the second tow-yo, the CTD was lowered off the stern A-frame; this greatly improved the manoeuvring of the ship.

Table 3.1 Locations of AVP Drops and CTD Casts

Site	Instrument	Drop	Date-Time (GMT)	Latitude (°N)	Longitude (°W)
0-1	AVP	432	920723-0927	32.65281	75.99849
0-2	AVP	433	920723-1216	32.63803	75.91115
0-3	AVP	434	920723-1509	32.63843	75.82133
0-4	AVP	435	920723-1829	32.61779	75.66413
0-5	AVP	436	920723-2156	32.63681	75.51919
0-5	CTD	16	920724-0146	32.627	75.5278
0-3	CTD	17	920724-0537	32.6394	75.8278
0-6	AVP	437	920724-0947	32.62722	75.34159
0-7	AVP	438	920724-1350	32.61824	75.12346
0-8	AVP	439	920724-1746	32.62487	74.93639
0-9	AVP	440	920724-2207	32.63280	74.63850
0-9	CTD	18	920725-0257	32.6543	74.6144
0-7	CTD	19	920725-0836	32.6076	75.1199
1-1	AVP	441	920725-1438	31.91537	75.49825
1-2	AVP	442	920725-1730	31.95694	75.41875
1-3	AVP	443	920725-2031	32.01381	75.34753
1-1	CTD	20	920726-0109	31.9023	75.4991
1-3	CTD	21	920726-0438	31.9934	75.3389
1-4	AVP	444	920726-0917	32.04948	75.26440
1-5	AVP	445	920726-1240	32.12079	75.22998
1-6	AVP	446	920726-1619	32.21442	75.12956
1-7	AVP	447	920726-2217	32.33664	74.96018
1-7	CTD	22	920727-0244	32.3368	74.9469
1-5	CTD	23	920727-0733	32.0961	75.2194
R-2	AVP	448	920727-1148	31.56654	75.14960
R-3	AVP	449	920727-1632	31.19045	74.81557
R-4	AVP	450	920727-2025	30.94249	74.56981
R-5	AVP	451	920727-2355	30.82247	74.47996
R-4	CTD	24	920728-0437	30.936	74.5651
2-1	CTD	25	920728-0943	30.6662	74.2626
2-1	AVP	452	920728-1124	30.64845	74.25540
2-3	AVP	453	920728-1522	30.70999	74.24535
2-5	AVP	454	920728-1912	30.72205	74.20667
2-7	AVP	455	920728-2243	30.77114	74.12888
2-7	CTD	26	920729-0315	30.7444	74.1304
2-5	CTD	27	920729-0657	30.7046	74.1958
2-2	AVP	456	920729-0931	30.66228	74.23898

Table 3.1 Locations of AVP Drops and CTD Casts (continued)

Site	Instrument	Drop	Date-Time (GMT)	Latitude (°N)	Longitude (°W)
2-4	AVP	457	920729-1258	30.71674	74.22066
2-6	AVP	458	920729-1705	30.72793	74.16284
2-6	AVP	459	920729-1705	30.72594	74.16405
2-8	AVP	460	920729-2113	30.77644	74.09055
2-8	CTD	28	920730-0147	30.7555	74.095
2-6	CTD	29	920730-0532	30.7395	74.1387
2-9	AVP	461	920730-0911	30.81082	74.02977
2-11	AVP	462	920730-1314	30.86629	73.94865
2-15	AVP	463	920730-2045	31.26464	73.28326
2-15	CTD	30	920731-0237	31.2522	73.3218
2-5	AVP	464	920731-0918	30.72107	74.18292
2-5	AVP	465	920731-1329	30.71964	74.18644
2-5	AVP	466	920731-1329	30.71814	74.18589
2-5	AVP	467	920731-1718	30.73074	74.19155
2-5	AVP	468	920731-1834	30.71476	74.20929
2-5	AVP	469	920731-2055	30.72706	74.19175
2-3	CTD	31	920801-0121	30.6967	74.2302
2-1**	CTD	32	920801-0438	30.6776	74.2534
3-2	AVP	470	920801-1446	30.56623	74.20497
3-1	AVP	471	920801-1550	30.59167	74.24533
3-3	AVP	472	920801-1947	30.43041	74.01333
3-4	CTD	33	920802-0243	30.2551	73.7704
3-5	CTD	34	920802-0727	29.9349	73.502
3-5	AVP	474	920802-1112	29.92873	73.50893
3-4	AVP	475	920802-1551	30.20887	73.74932
4-1	AVP	476	920802-1926	30.26018	73.86088
4-1	CTD	35	920803-0008	30.2681	73.8593
4-2	CTD	36	920803-0401	30.3041	74.0158
4-2	AVP	477	920803-0913	30.30369	74.02048
4-3	AVP	478	920803-1308	30.32741	74.15220
4-4	AVP	479	920803-1705	30.34642	74.33251
5-7	AVP	480	920803-2045	30.44006	74.31089
4-4	CTD	37	920804-0133	30.3493	74.3277
5-2	CTD	38	920804-0539	30.5683	74.2808
5-4	AVP	481	920804-0916	30.51144	74.27987
5-2	AVP	482	920804-1247	30.55785	74.29094
5-0	AVP	483	920804-1624	30.65674	74.32711

Table 3.1 Locations of AVP Drops and CTD Casts (continued)

Site	Instrument	Drop	Date-Time (GMT)	Latitude (°N)	Longitude (°W)
2-5	AVP	484	920804-1955	30.72281	74.18986
5-0**	CTD	39	920805-0105	30.6609	
5-3	AVP	485	920805-1240	30.53395	74.29675
5-5	AVP	486	920805-1612	30.47230	74.28764
2-3	AVP	487	920805-2018	30.70488	74.23435
2-7	AVP	488	920805-2346	30.77270	74.11630
	CTD	40	920806-0451	30.816	74.2505
	CTD	41	920806-0904	30.6484	74.1006
2-5	AVP	489	920806-1133	30.72343	74.18979
2-1	AVP	490	920806-1507	30.64481	74.26099
	AVP	491	920806-1822	30.64730	74.10370
2-5	AVP	492	920806-2151	30.72192	74.18794

** denotes tow-yo CTD casts

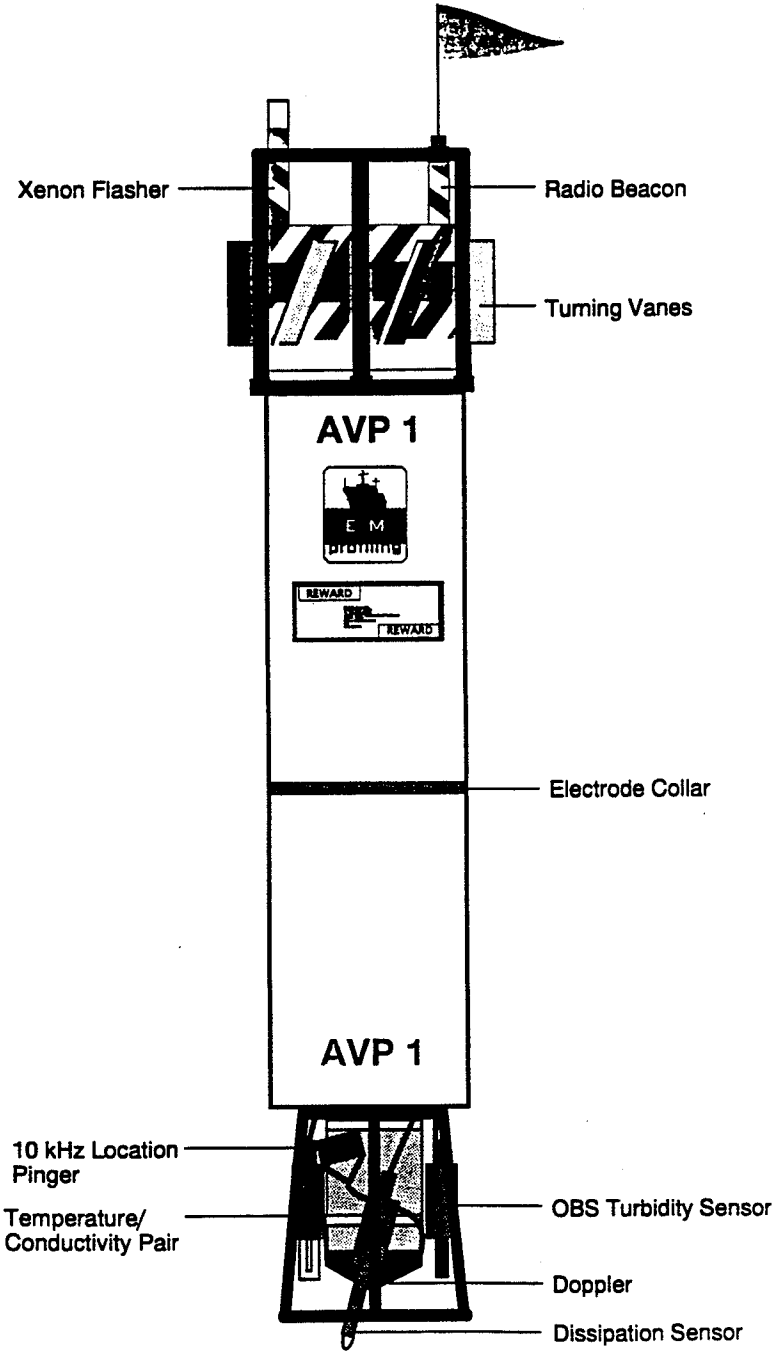

Figure 3.1. The Absolute Velocity Profiler (AVP) as used on cruise *Endeavor* 239. The electrode collar housed the 2-axis electric field array. The location pinger, xenon flasher and radio beacon facilitated recovering the Profiler.

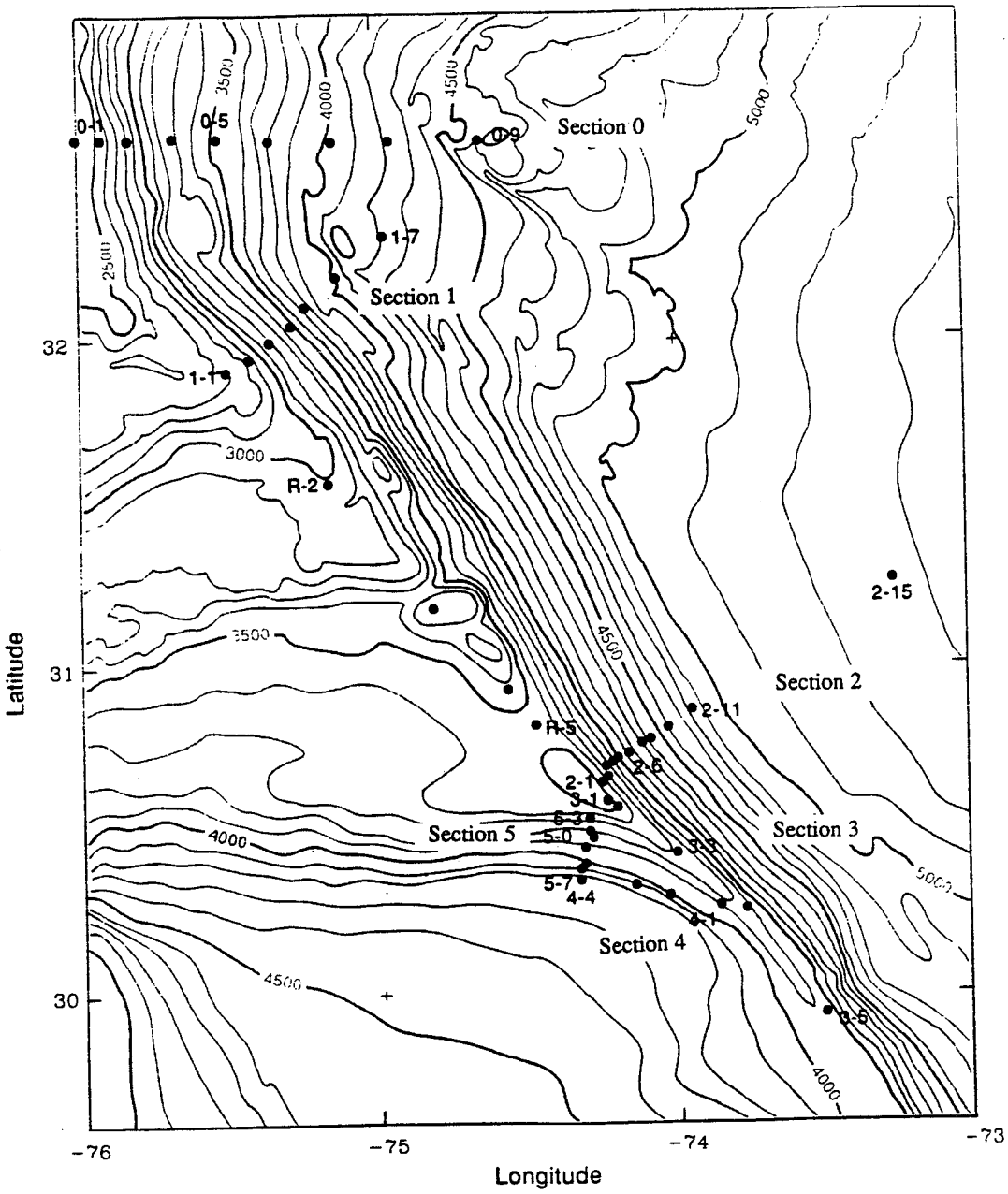

Figure 3.2. AVP and CTD profile locations. The label of each profile Site was constructed by starting with the Section number, followed by a hyphen and a Site number which increased with depth. Sites along the Ridge crest (e.g. R-2) begin with the Section letter "R". Additional sites were designated in the numbering scheme, but no profiles were made at these sites (e.g. Sites 2-12 to 2-14); these sites were not plotted. Bathymetry from the National Ocean Survey chart "Southeastern United States Regional Map" covering 25° N - 35° N, 72° W - 82° W.

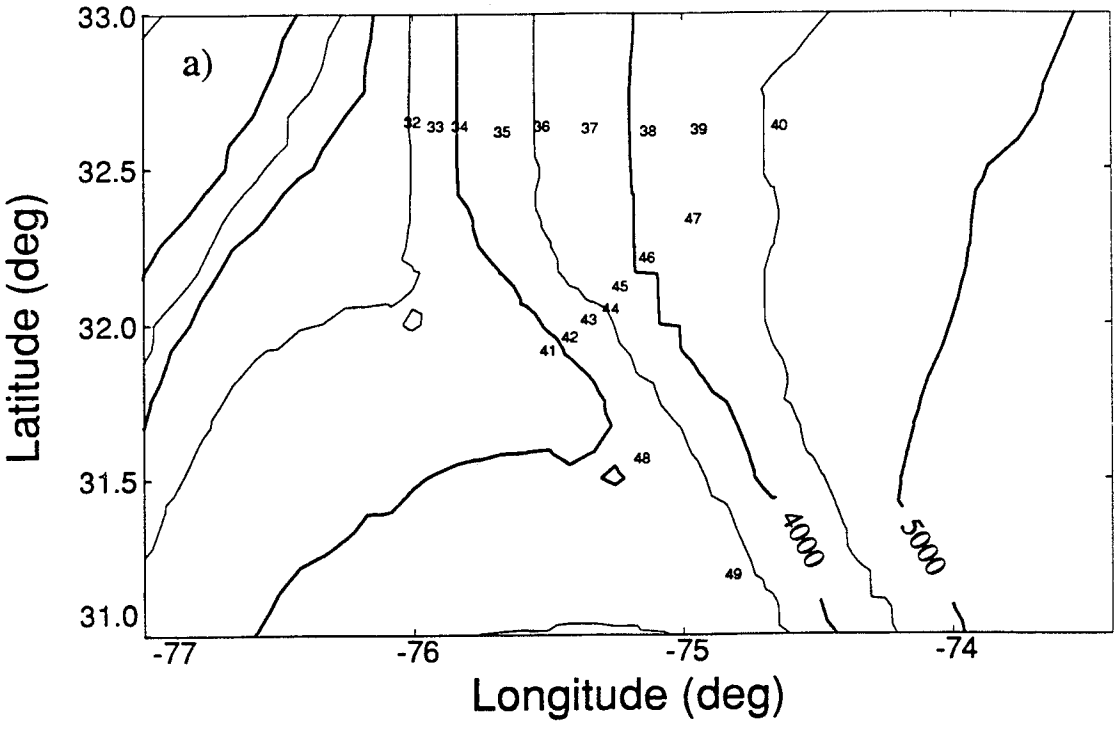

Figure 3.3. AVP drop locations. The labels on the plot have had 400 subtracted from the drop number. Bathymetry data set is DBDB5 from the National Geophysical Data Center.

a) AVP drops on Sections 0 and 1

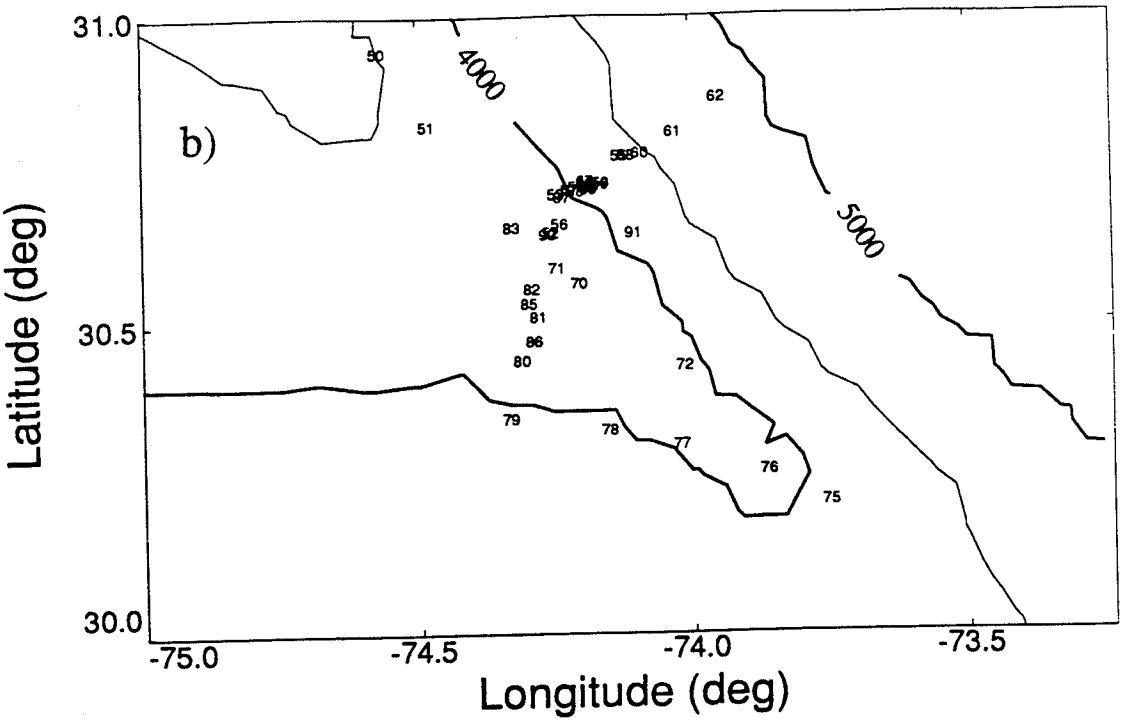

Figure 3.3. (continued) b) AVP drops on Sections 2, 3, 4 and 5

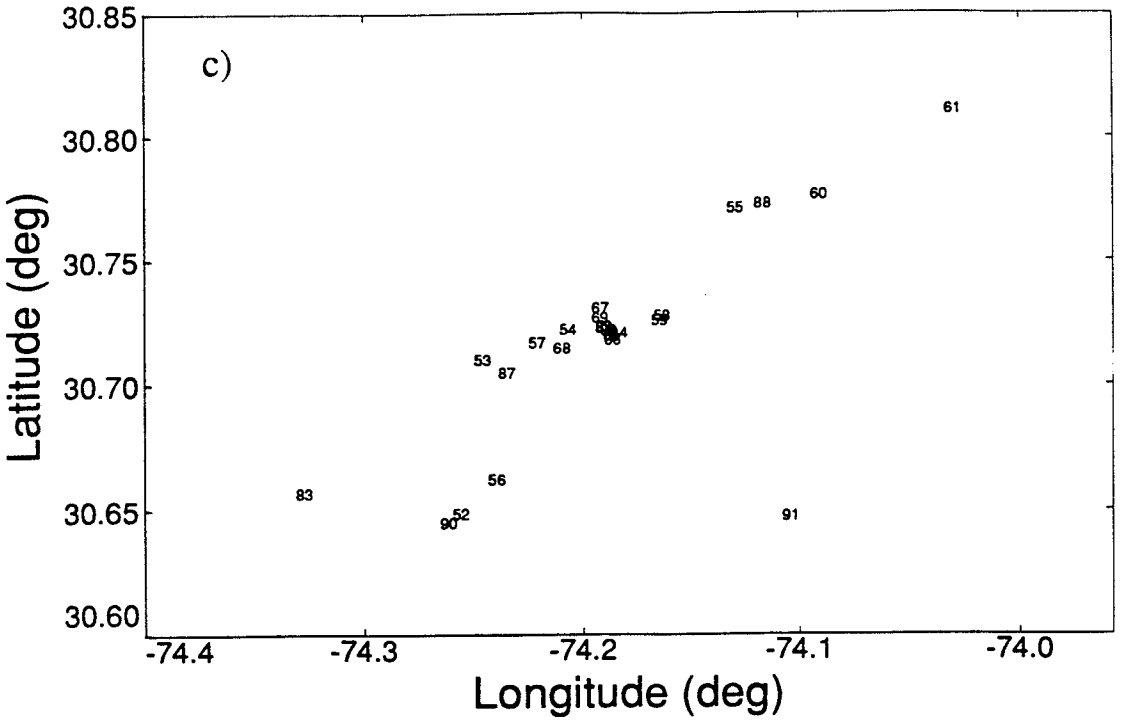

Figure 3.3. (continued) c) AVP drops on Section 2

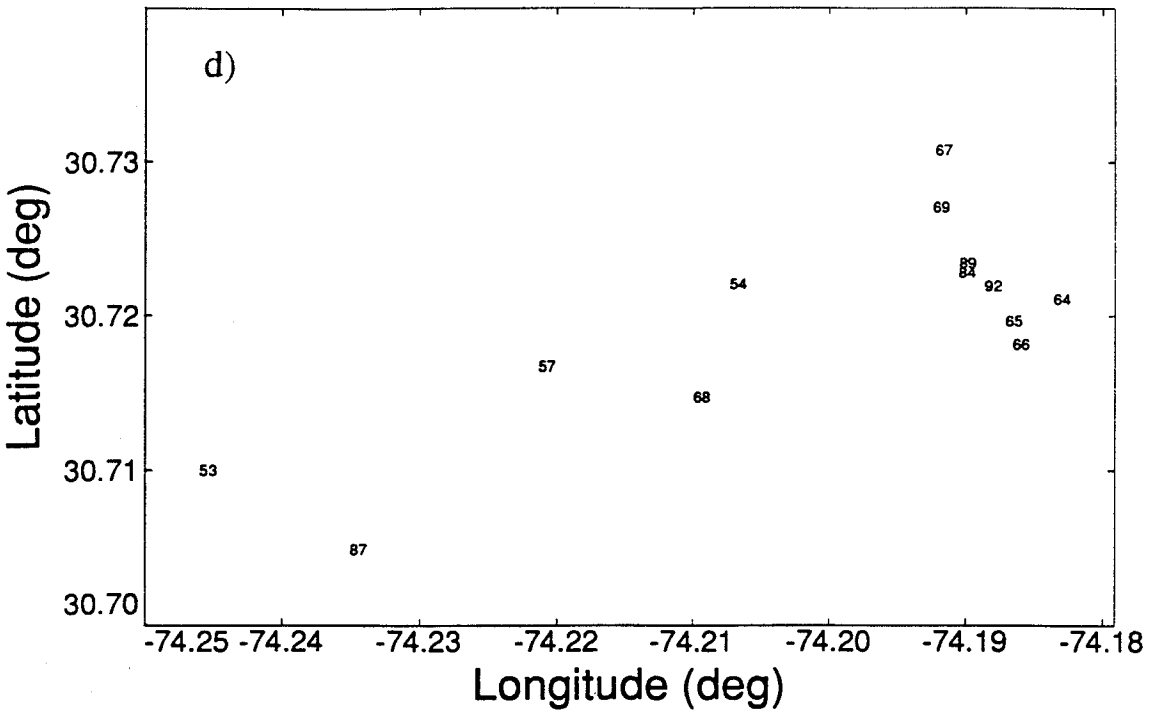

Figure 3.3. (continued) d) AVP drops near Site 2-5

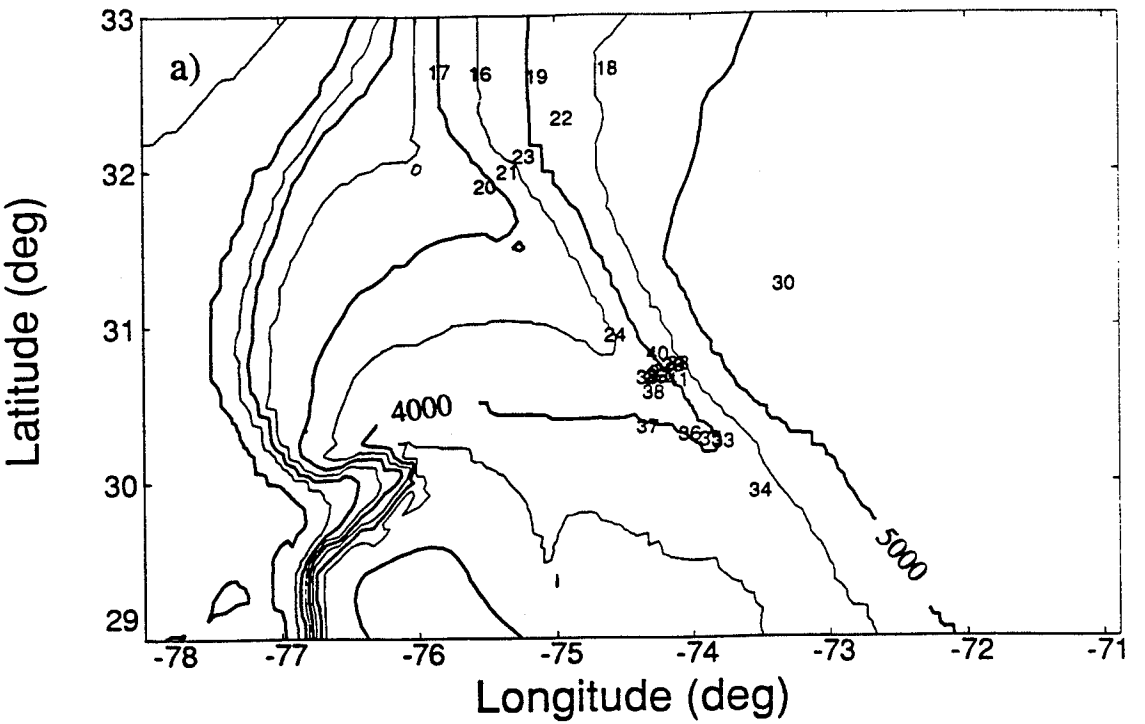

Figure 3.4. a) CTD cast locations. Detail of Section 2 is shown in b). Bathymetry data set is DBDB5 from the National Geophysical Data Center.

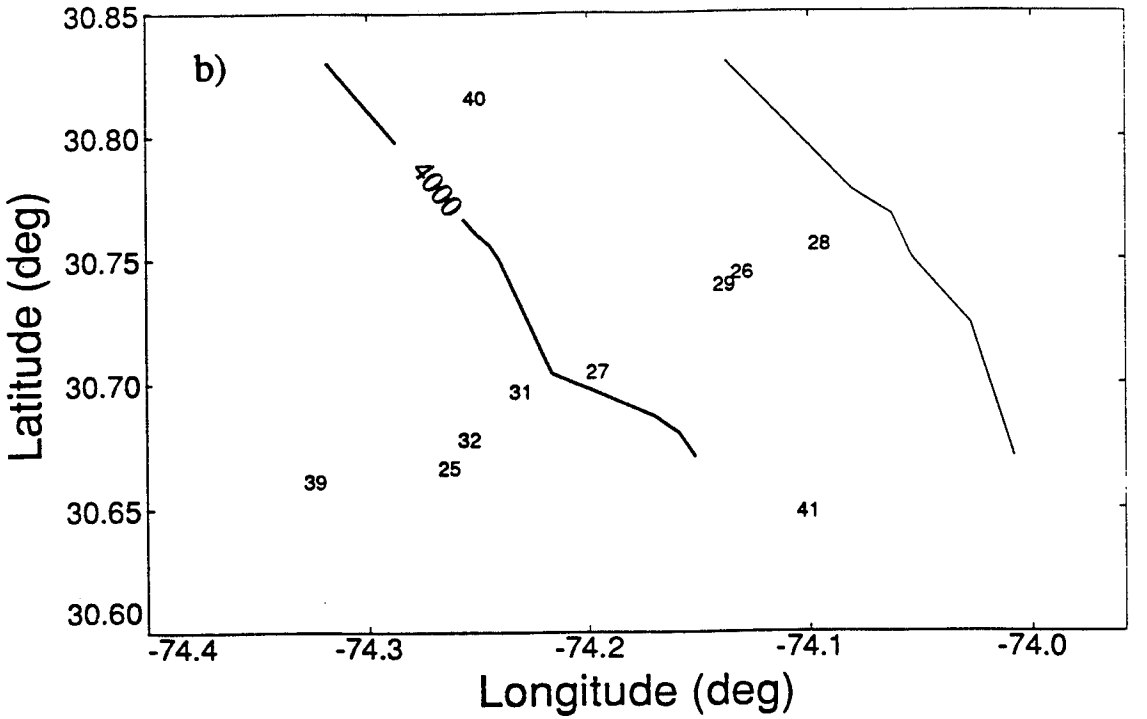

Figure 3.4. (continued) b) Detail of CTD cast locations on Section 2. CTD's 40 and 41 were 10 km upstream and downstream respectively of Site 2-5, the nominal drop site of CTD 27.

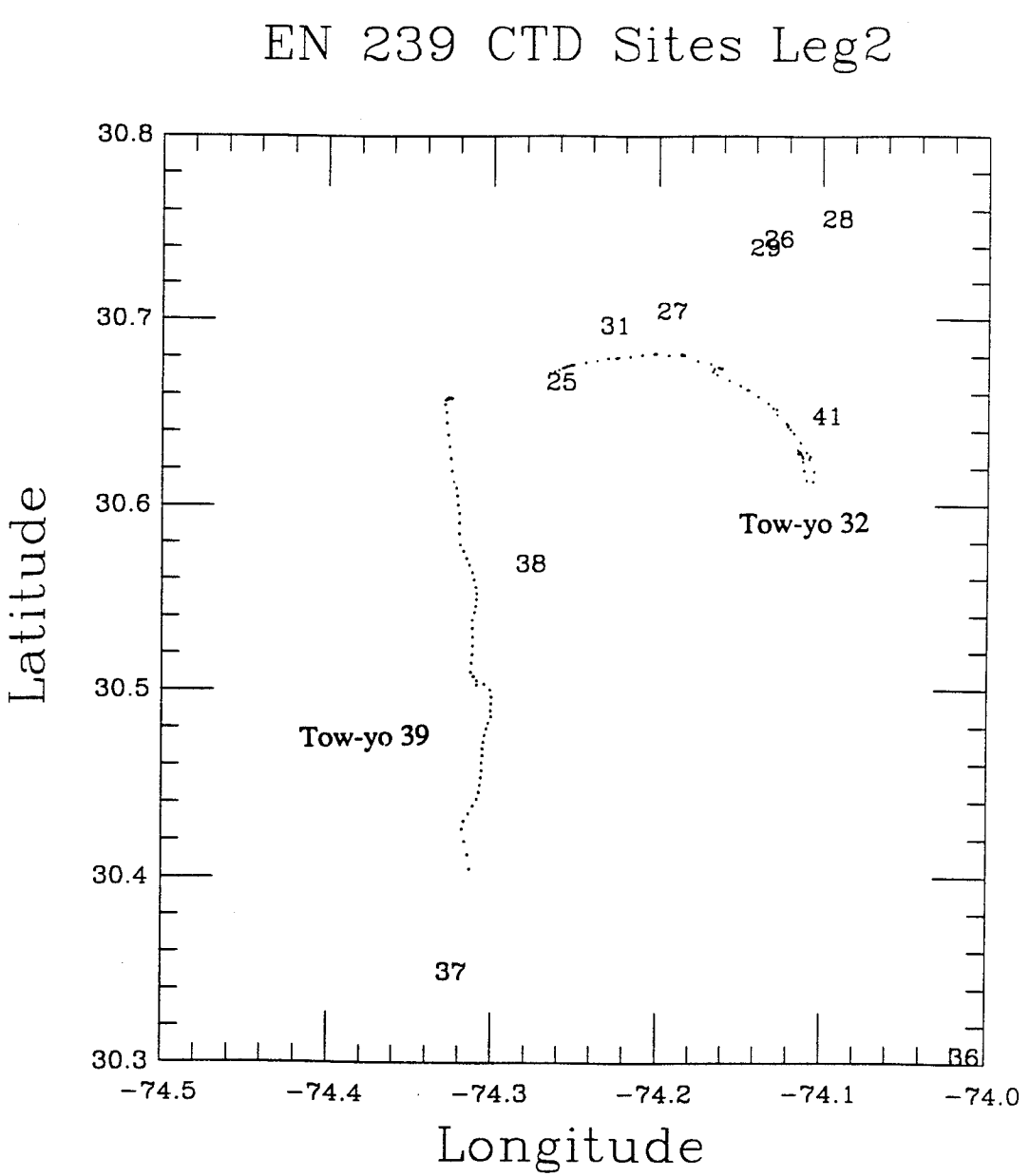

Figure 3.5. Ship's path for CTD tow-yo's 32 and 39 and cast sites for CTD's on Sections 2 and 5. Tow-yo 32 drifted to the south-east of Section 2 due to difficulty manouevering the ship with the CTD wire over the side.

Chapter 4. Analysis of the Bottom Boundary Layer

4.1 The Bottom Boundary Layer

The focus of this analysis of the EN239 cruise data from Leg 2 is on the bottom boundary layer (BBL). The Deep Western Boundary Current (DWBC) and the Blake-Bahamas Outer Ridge (BBOR) present a unique combination of deep, fast flow over a smooth sandy bottom. The largest features on the seafloor are sand waves which are themselves a regular feature caused by the current. The BBL at the Blake-Bahamas Outer Ridge is interesting because of its considerable thickness (up to 270 m) and remarkable homogeneity in water properties and flow speed; Figure 4.1 shows BBL profiles of velocity, potential temperature, and salinity. The BBL lent itself well to study since it was in a relatively confined area of the ocean and, at various locations along the BBOR, presented a wide range of speeds and thicknesses for comparison. Figure 4.2 shows the velocity averaged over the bottom 100 dbar (usually the BBL thickness was greater than 100 dbar). In general, the flow followed the contours of the seafloor, with the exception of those stations near the ridge crest.

Figure 4.3 shows contours of potential temperature, salinity and potential density for a line along Sections 2 and 5. (The potential temperature and density were referenced to 4000 dbar.) Data from Section 5 are on the left side of the plot; the DWBC flow is into the paper. On the right side of the plot is Section 2 on the NE side of the Ridge; the flow is out of the page. Because Section 2 was not co-linear with Section 5 (see Figure 3.2), there is a fold of about 50 degrees in the contour plot at 0 km distance. The numbers along the top of each plot are drop numbers of AVP profiles and indicate the locations at which the profiles were made. These contour plots show the slope of water properties in the DWBC; the slopes were nearly parallel to the bottom on either side of the Ridge. Within approximately 200 dbar of the bottom, the water in the BBL was nearly homogeneous and was cooler and fresher than the overlying stratified water. In Figure 4.3c, the water in the BBL on the upstream side of the Ridge (Section 2) was slightly denser, $O(0.002\ \mathrm{kg/m^3})$, than on the downstream side. However, this slight difference in density might result merely from the time difference between the surveys of the two sections. This figure also shows that the BBL thickness remained constant after the DWBC rounded the crest of the Ridge.

There was not only remarkable vertical homogeneity of water properties in the BBL, but also considerable homogeneity in the across-slope direction. The CTD tow-yo surveys of the BBL (Figure 4.4) gave more detail of the lateral gradients in the BBL; the surveys of each side of the Ridge were made in one night each, so the view of the BBL on either side of the Ridge was almost instantaneous. In the absence of any flow in a stratified ocean, we would expect the across-slope gradient in the BBL on a sloping bottom to result from the intersection of the oceanic vertical gradient with the inclined seafloor. However, the lateral gradients in Figure 4.4 were an order of magnitude smaller than this simple estimate predicts.

To look at these gradients in the BBL quantitatively, rather than qualitatively on a contour plot, we plotted these properties as a function of distance along Section 2 (Figure 4.5). The dots in Figure 4.5 show the average BBL water properties at each AVP Site along Section 2, with the exception of the deepest AVP profile at Site 2-15, AVP drop 463. The solid line in Figure 4.5 is a lateral projection of AVP drop 463 onto the Ridge and shows the cross-slope gradients expected in the absence of flow. This figure shows that the measured cross-slope gradients along Section 2 were lower than the projection of the external gradients. Note that the changes in salinity and temperature across the slope produced opposite changes in the density so that the gradient in potential density was smaller than if the salinity in the BBL had not been decreasing in the down-slope direction.

Since the cross-slope gradient of potential density was small, the slippery boundary layers proposed by MacCready and Rhines (1991) did not exist at the Blake-Bahamas Outer Ridge. After these data were collected, Garrett, MacCready and Rhines (1993) pointed out that little shut-down by way of arrested Ekman layers is expected to occur when the interior isopycnals tilt up with a slope almost equal to that of the bottom. In hindsight, the Blake-Bahamas Outer Ridge was not a suitable location to look for slippery bottom boundary layers.

One possible mechanism for producing these low cross-slope gradients is a secondary circulation within the BBL. This circulation moves and mixes the water in the BBL up and down the slope in the following manner. A near-bottom Ekman flow, created by the DWBC flowing over a frictional bottom, carries fluid (within approximately 20 m of the bottom) down the slope; this transport is balanced by a return flow up-slope in the upper portion of the BBL. Such a circulation could not exist if the

initial cross-slope potential density gradient in the BBL were large enough so that buoyancy effects could shut down the Ekman transport in the manner proposed by MacCready and Rhines (1991).

There is another possible reason for the cross-slope gradients observed in the BBL being so small. The geostrophic tilt of the isopycnals causes a low cross-slope gradient in the waters above the BBL. In Sections 2 and 5, the isopycnals were almost parallel to the bottom (Figure 4.3c). Since the water above the BBL was essentially the same potential density at any position across the slope, the water mixed down into the BBL would also be of uniform density; hence the BBL would have correspondingly small cross-slope gradients.

4.2 The Bottom Boundary Layer Thickness

In the majority of the 60 AVP profiles of the DWBC, there was a thick bottom boundary layer that was homogeneous in water properties (e.g. Figure 4.1). Potential temperature and salinity were well-mixed to the same height above the bottom for any given profile; in the following discussion, the bottom boundary layer thickness was based on the height above the bottom at which the potential density began to decrease. In comparisons of profiles of velocity, temperature and salinity (e.g. Figure 4.1), the velocity was usually constant in the BBL except for a near-bottom shear layer within 60 m of the bottom; this was coincident with the region of high dissipation rate near the seafloor (Figure 4.6a). In addition, the shear above the BBL was very low.

Figure 4.7 shows the distribution of the bottom boundary layer thickness at each AVP profile location; the maximum thickness of the BBL was 270 m. In the remainder of this Section, we discuss the parameterization of the BBL thickness for each AVP profile, with the following exceptions. The BBL thickness was essentially zero at both ends of Section 0 and at the deep end of Section 2, although the flow speeds there were not zero. These profiles were not within the DWBC, so it is possible that the flows were too transient to develop measurable BBL's.

Garrett (1990) predicted that the boundary layer thickness, h, is

$$h = -\,Pr\,\varepsilon^{-1}\,f^{-1}\,U(\infty)\,\tan(\theta)$$

where ε depends on the buoyancy change across the boundary layer and the buoyancy frequency N, Pr is an eddy Prandtl number, f is the Coriolis parameter, $U(\infty)$ is the far-field alongslope flow, and θ is the angle of inclination of the seafloor. If we assume, for simplicity, that Pr, f and ε are constant, then the BBL thickness depends only on the product of U and $\tan(\theta)$. The correlation between speed × bottom slope and thickness was poor for Sections 0 and 1 (Figure 4.8). The correlation was much better on Sections 2 and 5 where the flow was fast. The data from Sections 3 and 4 are grouped to the left side of Figure 4.8 since the bottom slope was small (and the flow was stalling as it crossed the Ridge on Section 3) and yet the BBL maintained its thickness.

However, this test of Garrett's model was not rigorous since the assumption that Pr and ε were constant was made without any sound basis. To make a full evaluation of this model, it will be necessary to calculate ε from each density profile and to estimate an eddy diffusivity and an eddy viscosity (to calculate the eddy Prandtl number) for each AVP drop.

Models of BBL thickness, such as Garrett's above, depend solely on the instantaneous local geometry of the boundary and dynamical properties of the flow. Such a model might be applicable in a steady-state flow over a seafloor of uniform slope. However, in the case of a variable flow over complex topography, we propose that thickness of the BBL will depend additionally on the history of the flow. Moreover, near the Ridge crest, the BBL thickness might be affected by the stalling of the flow and horizontal leakage of the BBL across the Ridge crest.

4.3 Vertical Homogeneity in the Bottom Boundary Layer

As we have noted in Section 4.1, the BBL was remarkably homogeneous in temperature, salinity and density. However, there was an irregular feature in the BBL which appeared in approximately half of the AVP and CTD profiles. The temperature and/or salinity profiles increased or decreased slightly in the middle of the BBL (e.g. Figure 4.9) so that there seemed to be two well-mixed layers, one above the other. These steps in water property profiles appeared in data from different sensors on different instruments, so it is unlikely that these steps were an artifact of a poorly

functioning sensor. Steps in temperature and salinity in the primary CTD sensor data also appeared in the secondary sensor data.

The sensors used on the CTD and AVP were highly accurate "state of the art" devices, used with careful calibration. In addition, the AVP data were not subject to noise due to ship heave as the CTD data were. The steps were first observed in the AVP data and only then found in the CTD data by smoothing the data.

Changes in temperature at a step were on the order of 0.001 °C or larger (up to 0.006 °C in AVP drop 491); the accuracy of the temperature measurements was better than 0.001 °C overall, and in the bottom boundary layer, the performance of the sensors was optimal since the overall changes in temperature were very small and the instrument was well equilibrated to its surroundings. In a well-mixed BBL away from any steps, the peak to peak noise in a typical temperature profile was 0.0002 °C; the data in these profiles were averaged over 4 dbar bins. Since the temperature in these profiles was constant over $O(100)$ m depth, this noise level represents an upper bound on the precision of the temperature measurements in the BBL.

Changes in salinity at a step were usually in the range of 0.0005 to 0.001 PSU. The peak to peak noise in the salinity profiles was 0.0002 PSU.

We looked at all of the AVP drops and CTD casts to see how frequently these steps occurred and what types of steps existed. In 13 AVP profiles and 11 CTD profiles, the potential density was unstable across the steps (e.g. Figure 4.10c). The density was stable at the step in 8 AVP drops and 4 CTD profiles. The BBL was homogeneous (without steps) in 17 AVP profiles and 4 CTD casts. Not included in these counts are the two tow-yo's which each contained many profiles through the BBL. The overall difference between these tow-yo's is that in Section 5 (CTD 39) the BBL was generally homogeneous and in Section 2 (CTD 32) there were several profiles which showed steps in temperature or salinity in the BBL. This difference might be a result of enhanced mixing as the DWBC crosses the Ridge crest.

The transmissivity profile (Figure 4.10d) shows qualitatively the amount of forward scattered light travelling from the emitter to the receiver of the transmissometer on the CTD. The more suspended sediment in the water, the lower the transmissivity. CTD 31 (Figure 4.10) shows an unstable step with no change in the level of suspended sediment; this is typical of the unstable steps seen in the CTD data. However, in two of

the CTD casts with unstable profiles in the BBL, there was an increase in suspended sediment in the lower layer. CTD 26 (Figure 4.11) is an example of this type of step in the BBL. The potential density is calculated only from the water properties; the sediment concentration is not included in the calculation. An increase in suspended sediment tends to increase the density, so the step in Figure 4.11 might not actually be unstable.

There was an increase in noise in the data between the AVP (Figure 4.9) and the CTD (Figure 4.10). In particular, we attribute the sinusoidal variability in the CTD profiles (Figure 4.10) to acceleration of the sensors due to the heaving motion of the ship. We think that this acceleration caused variability in the flow rate of water past the sensors. This noise was seen in both primary and secondary sensors. The AVP fell freely through the water, and the superior data quality of the AVP reflected this advantage.

We observed examples of sharp steps with strong gradients and examples of steps with weak gradients. In the case of the sharp steps, the two layers must have recently come into contact, since the step had not yet been smoothed by diffusion or, in the case of unstable profiles, by buoyancy effects.

One possible means of producing an unstable profile in the BBL is for the water to overturn so that light fluid above the BBL is captured in the bottom portion of the BBL. Figure 4.10 is interesting because it shows an example of an unstable profile which could not have been produced by this process, since the salinity near the bottom was less than the salinity above the BBL.

We can not estimate the turbulent diffusion of the steps since the dissipation rate observations were moderately noisy. The dissipation profile in Figure 4.6a shows a noise level of approximately 3×10^{-9} W kg^{-1} at depths less than 4000 dbar; this noise level was typical of the profiles,

We can, however, put an upper limit on the time for unstable density steps in the BBL to dissipate. If we ignore turbulent dissipation, we can estimate the time scale for the buoyancy difference across an unstable step to overturn the boundary layer. The buoyancy frequency, N, is given by

$$N^2 = -\frac{g}{\rho}\frac{d\sigma}{dz}$$

where σ is potential density and z is height relative to the sea surface. To estimate the time scale involved, we set $d\sigma$ to be the density difference across the step and dz the BBL thickness; since the step is unstable, N^2 is negative. For CTD 31 (Figure 4.10), $d\sigma$ is 0.0004 kg/m^3, dz is 200 m and the time scale for this density profile to overturn is

$$\frac{1}{\sqrt{-N^2}}$$

or approximately 2 hours.

We also noticed that although the steps in the BBL seemed intermittent, there were locations where successive profiles indicated the same structure in the BBL. For example, AVP drop 455 (Figure 4.12) profiled the BBL 3 hours before CTD 26 (Figure 4.11). The AVP drop was 1.8 km from the CTD cast. Both temperature profiles show a 0.002 °C decrease with height 35 dbar above the bottom. While we cannot say that the feature seen in one profile is related to the other, we can say that if this is the same feature, then such features have a time scales of at least 3 hours, a length scale of 1.8 km in the cross-slope direction, and a length scale of 1.6 km in the along-slope direction, because this feature was advected by a flow of 15 cm s^{-1} in the 3 hours between the two profiles. Eight days later, this step was not present in the next drop at this site (AVP drop 488, Figure 4.9).

4.4 Topographic Rossby Wave Interaction with the BBL

Freely propagating Rossby waves which impinge on sloping topography are transformed into topographic Rossby waves (TRW's). The beta effect which provides the restoring force for Rossby waves is augmented by a "topographic beta" effect. Horizontal motion in the Rossby wave is impeded near the bottom by the presence of the Ridge. In addition, because the ocean is stratified, fluid columns that have been pushed upslope by the wave motion slosh back down because of buoyancy effects. This sloshing motion is continuously repeated at the frequency of the original Rossby wave. Thus the Rossby wave is refracted by sloping topography and becomes a topographic Rossby

wave.

According to theory (Rhines, 1970) in the case of an ocean with constant buoyancy frequency, N, a topographic Rossby wave on a sloping wall has a velocity structure that is an hyperbolic cosine in the vertical. Such waves were observed at the BBOR. (There are also higher order theoretical modes in which the vertical structures are cosines, but these modes were not observed at the BBOR, and so we are concerned here only with the "barotropic" mode.) The vertical structure depends on the wavelength of the wave, the slope of the bottom and the orientation of the wave relative to the gradient of the seafloor.

Data from three current meters on a mooring located at our Site 2-5 (Mills and Rhines, 1979) indicated an oscillating flow with a period of 19 days; the velocity vectors veered in an ellipse with major axis roughly aligned with the bottom contours. The vertical structure of the variability of the along-slope flow speed agreed well with the theoretical hyperbolic cosine for TRW's (Figure 4.13). Following Pickart and Watts (1990), we identified this variability as topographic Rossby waves; the reader is cautioned that this variability might be due to some other periodic motion with the same vertical structure. Based on these data, we anticipated strong TRW currents and, therefore, during the experiment, we surveyed Section 2 twice and made repeated profiles at Site 2-5 to resolve the spatial and temporal structure of TRW's. We did see TRW vertical structure (Figure 4.14) in velocity profiles from EN 239 on Section 2. Interestingly, we did not observe TRW's on the other side of the Ridge at Section 5. Section 5 must be in the shadow of the BBOR from the source of the TRW's. The source of wave energy must therefore be to the north and/or east of the Ridge. Rossby waves generated by meanders of the energetic Gulf Stream are a likely source of these waves.

In addition to the TRW vertical structure of the velocity profiles, we also observed properties of TRW's in the BBL. The water properties in the BBL changed in time, and we show here that this change was consistent with the TRW moving the BBL up-slope. Unfortunately, we observed less than a half period of the wave, so we did not see the TRW flow moving the BBL back down slope. However, buoyancy considerations alone imply that this up-slope motion of the BBL could not be steady in time.

At Site 2-5, where we had the longest time-series, the BBL became steadily cooler and fresher over the course of the experiment (Figure 4.15). Not included in this plot are three AVP drops at Site 2-5: AVP drop 454 was in shallower water than intended, and AVP drops 466 and 468 were made with the second profiler, AVP2, because these data contained noise spikes. These data are useful for determining the accuracy of the AVP sensors. The four earliest points in Figure 4.15 show four individual profiles at the same site over a 12 hour period. Because these data represent an average over 100 m, the precision of these averages was high. The peak to peak displacement of the four potential temperature measurements about a linear regression to the time-series was 0.001 °C, so the precision of these measurements is one third of that, or 0.0003 °C rms. Similarly, the precision of the salinity averages was 0.0003 PSU rms. It is important to note how close the changes in salinity and temperature over the entire time-series were to the accuracy of the sensors. In Figure 4.15, the salinity changed by about 0.002 PSU over 150 hours at Site 2-5, which was one order of magnitude greater than the precision given above. By comparison, the change in temperature was 0.012 °C, which was 30 times the precision of the measurement. We chose potential temperature for looking at the rate of change of BBL properties. The rate of change of potential temperature at Site 2-5 (from a least squares linear fit to Figure 4.15) was 8×10^{-5} °C/hr.

We interpreted this change in temperature at Site 2-5 as a lateral movement of a frozen-field BBL. To confirm this, we compared the relationship of potential temperature versus salinity for Site 2-5 and the first survey of Section 2 (Figure 4.16a). The theta-salinity values for Site 2-5 were in good agreement with Section 2, so these data supported the hypothesis that the BBL moved up-slope past Site 2-5. It is possible that along-slope gradients in the BBL advected past Site 2-5 could have produced the temporal changes in water properties that we observed at Site 2-5. However, a comparison of Sections 0, 1 and 2 (Figure 4.16b) shows that, in each of the Sections, the BBL properties fell near the same line in the plot of potential temperature versus salinity. As a cautionary note, although Sections 0 was O(200 km) up-stream from Section 2, the BBL that we observed in Section 0 was advected to Section 2 between our first and last surveys of Section 2; we can only estimate the time at which this water arrived at Section 2 since we have velocity measurements only at each Section. Therefore, the along-slope distance (in the moving frame of the BBL) between the water observed in the three Sections in Figure 4.16b is considerably less than the actual distance between the Sections. These data do not rule out the possibility of along-slope gradients in the

BBL, but they show the uniformity of the BBL and indicate that the changes in temperature and salinity that we observed at Site 2-5 were more likely due to the up-slope movement of the BBL.

Next, we determined the cross-slope temperature gradient on Section 2 and inferred the rate of up-slope motion from the ratio of the rate of change of temperature at Site 2-5 to the horizontal gradient. Figure 4.17 shows a plot of potential temperature versus across-slope distance for Section 2. The temperature plotted was actually the average of the bottom-most 100 dbar of the temperature profile; the potential temperature was essentially constant over this depth range of the BBL, within the resolution of the Sea-Bird temperature sensors. The line plotted through the data was the least-squares fit to the AVP data. The CTD data are shown only for comparison; CTD 27 was near Site 2-5. The cross-slope temperature gradient was 0.0034 °C/km. If the BBL was a frozen field which was advected up-slope past Site 2-5, then the cross-slope velocity was $(8 \times 10^{-5}$ °C/hr) / (0.0034 °C/km) = 0.02 km/hr or 0.6 cm/s.

The measured cross-slope velocities for each of the AVP profiles at Site 2-5 (Figure 4.18) were too noisy to compare with the velocity of 0.6 cm/s determined by the temperature gradient technique above. The scatter in the cross-slope velocity was 1.5 cm/s and further error was introduced by the uncertainty in the direction of the bottom slope. For a flow speed of 25 cm/s, an estimated 5 degrees uncertainty in the orientation of the topographic slope resulted in 2 cm/s uncertainty in the cross-slope velocity. The uncertainties in the AVP cross-slope velocities were too large to make a conclusive comparison with the velocity determined by the temperature method.

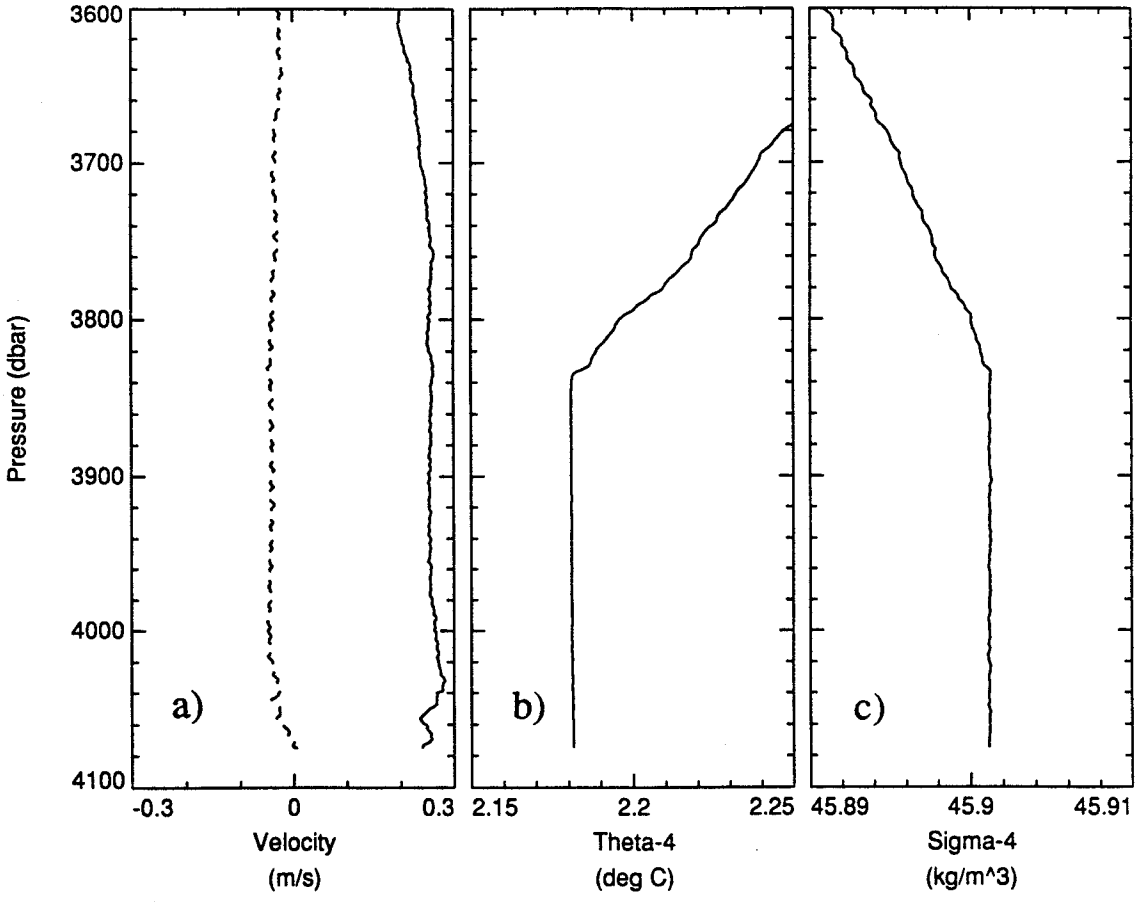

Figure 4.1. Profiles of a) velocity, b) potential temperature and c) potential density in the bottom boundaray layer from AVP drop 484. The solid line in a) is the along-slope flow. The dashed line is the down-slope component of the flow; this component is negative, so the flow is actually directed up the slope.

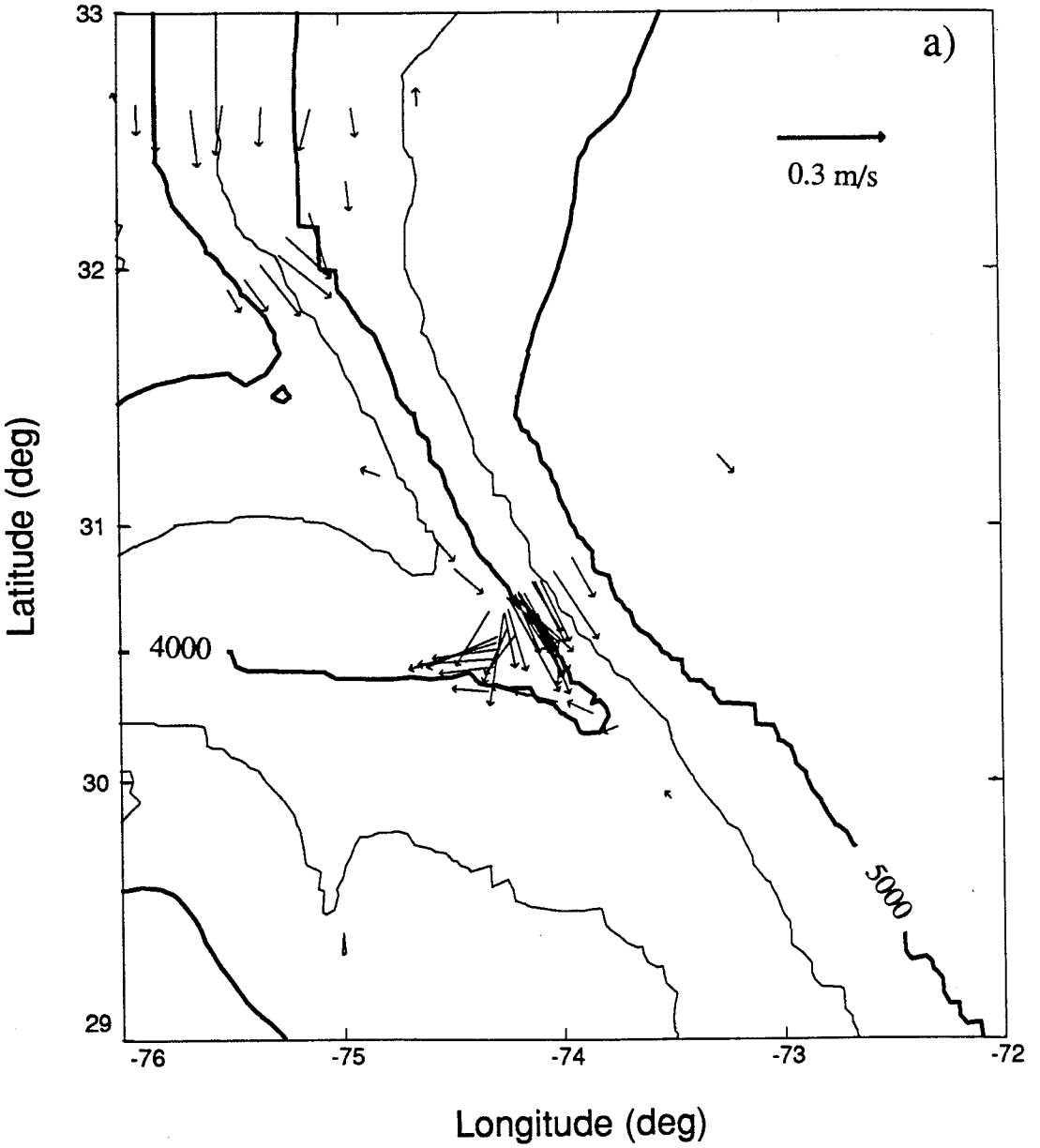

Figure 4.2. a) Near-bottom flow for each AVP drop. The velocity vectors represent the average flow from the bottom 100 m of each profile. The tail of each arrow is at the profile location. Bathymetry data set is DBDB5 from the National Geophysical Data Center.

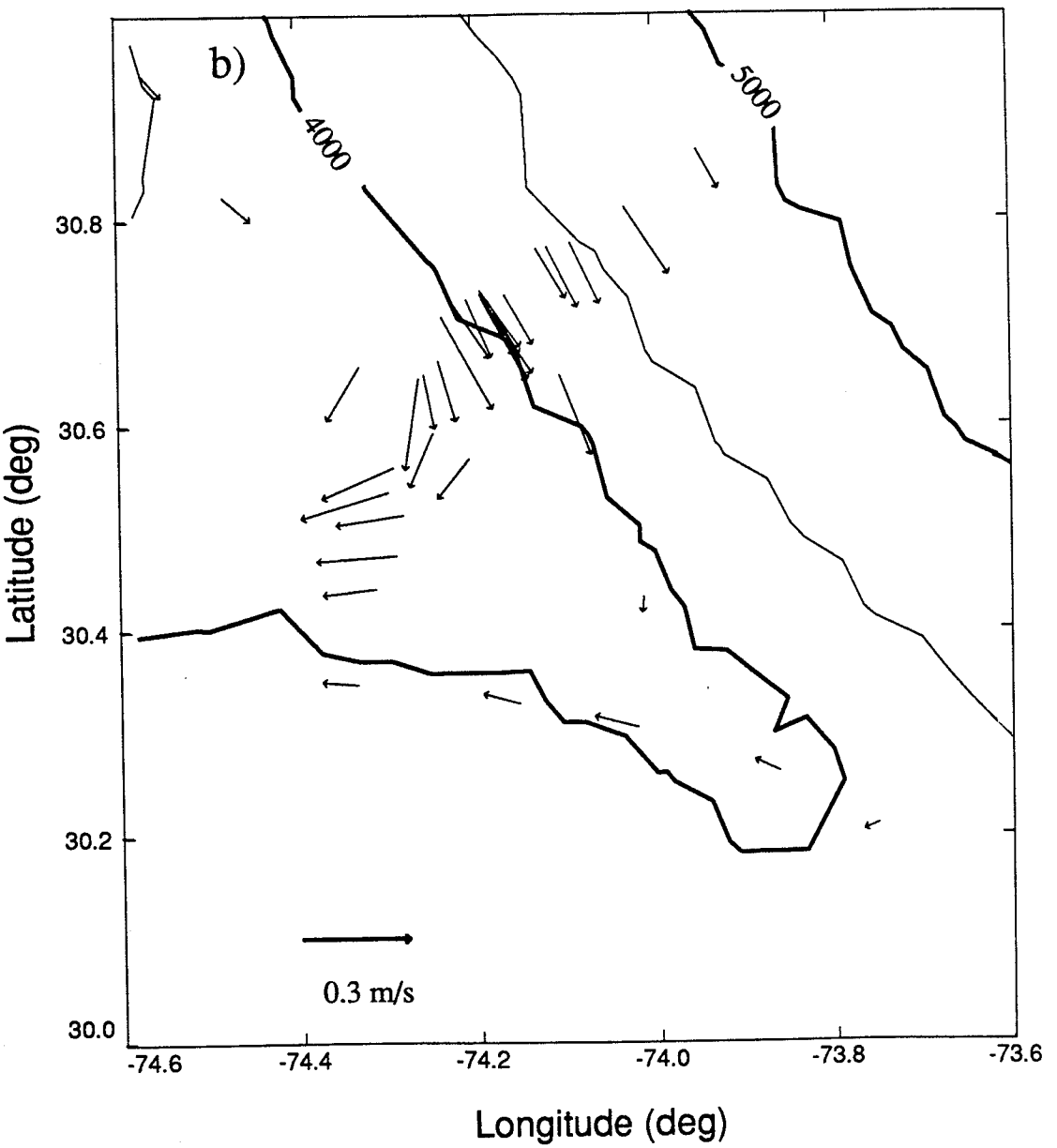

Figure 4.2. (continued) b) Detail of near-bottom flow around the Ridge crest. The velocity vectors represent the average flow from the bottom 100 m of each profile. The tail of each arrow is at the profile location.

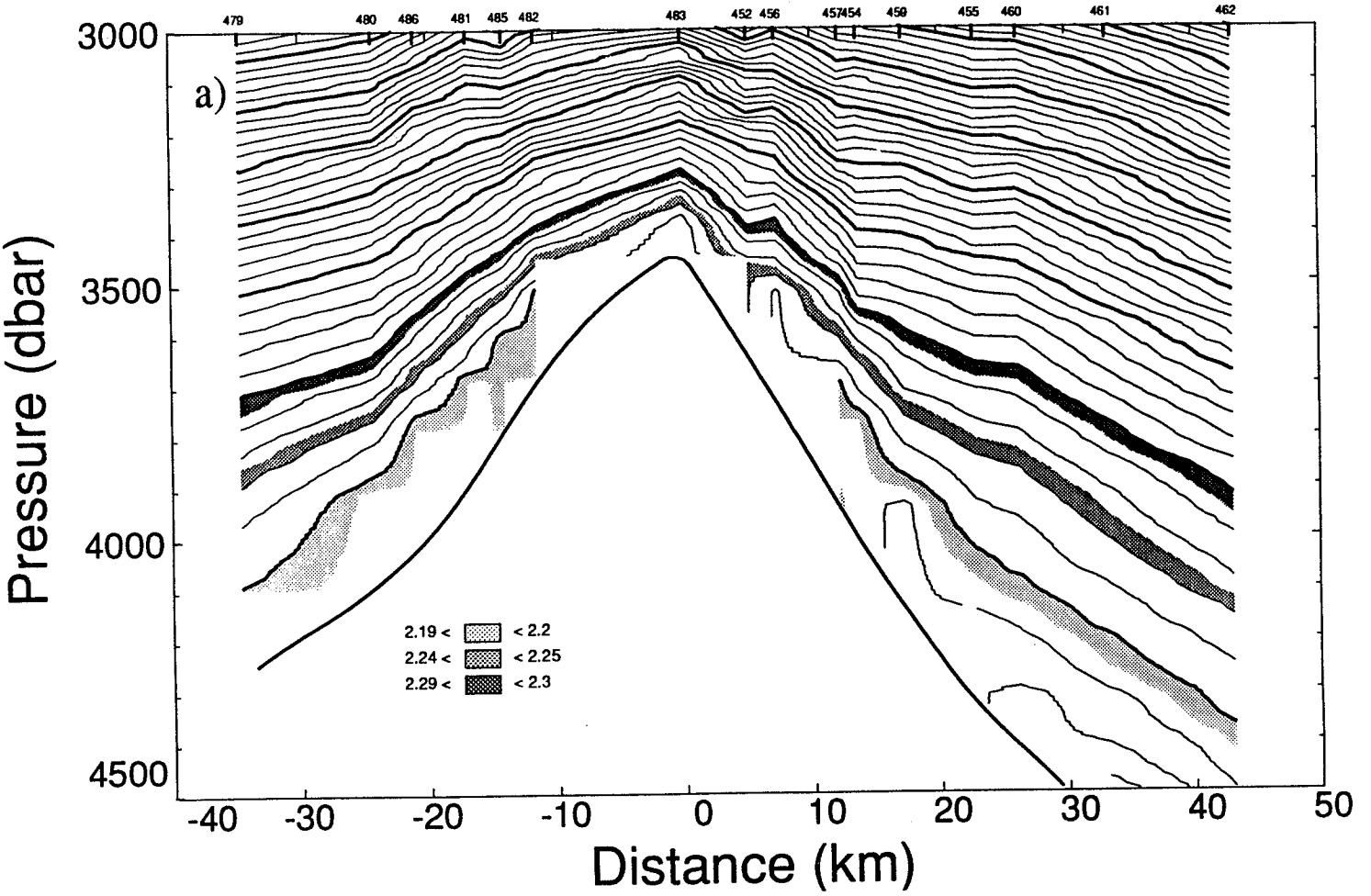

Figure 4.3. Contours of AVP data from Sections 2 and 5. The left side of the plot is Section 5 and the right is Section 2. The dark line under the contours is the topography. The AVP drop numbers listed across the top of the plot indicate the drop locations. a) Potential temperature. Contour interval is 0.02 °C.

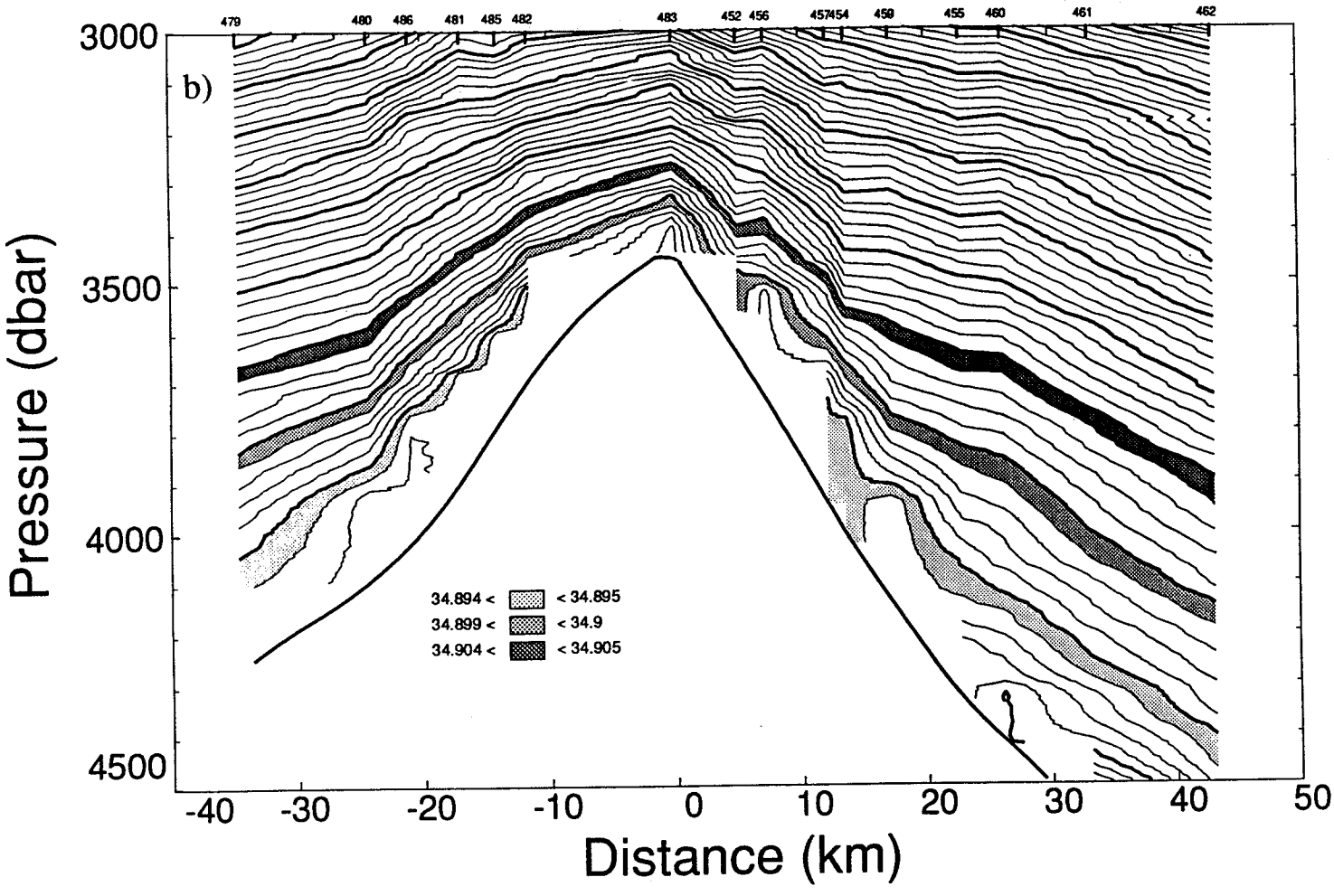

Figure 4.3. (continued) b) Salinity. Contour interval is 0.001 PSU.

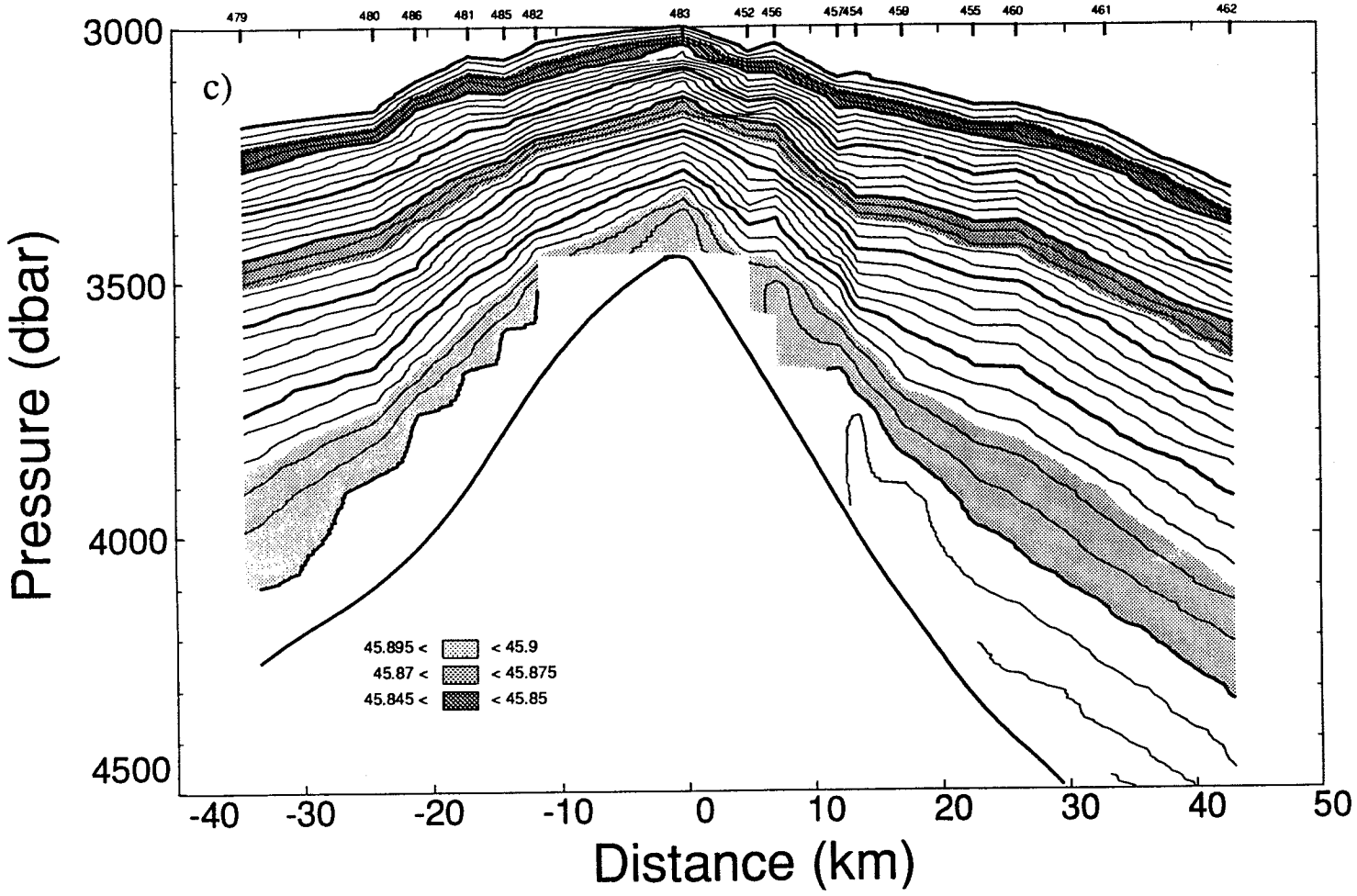

Figure 4.3. (continued) c) Potential density. Contour interval is 0.002 kg m^{-3}.

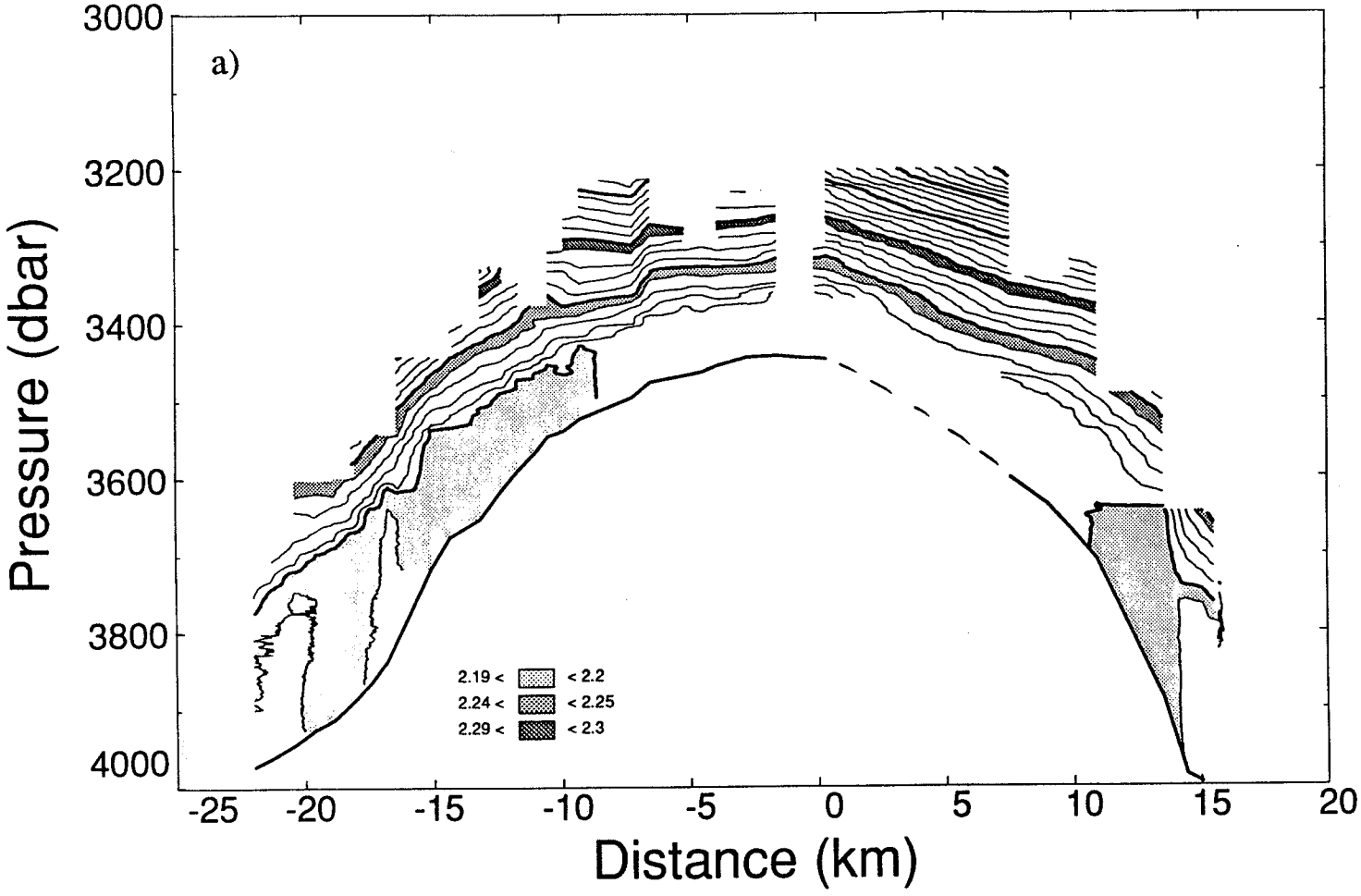

Figure 4.4. Contours of CTD data from tow-yo's on Section 2 (CTD 32) and Section 5 (CTD 39). The left side of the plot is Section 5 and the right is Section 2. The dark line under the contours is the topography. The data between 0 and 7 km are interpolated between the tow-yo's. a) Potential temperature. Contour interval is 0.01 °C.

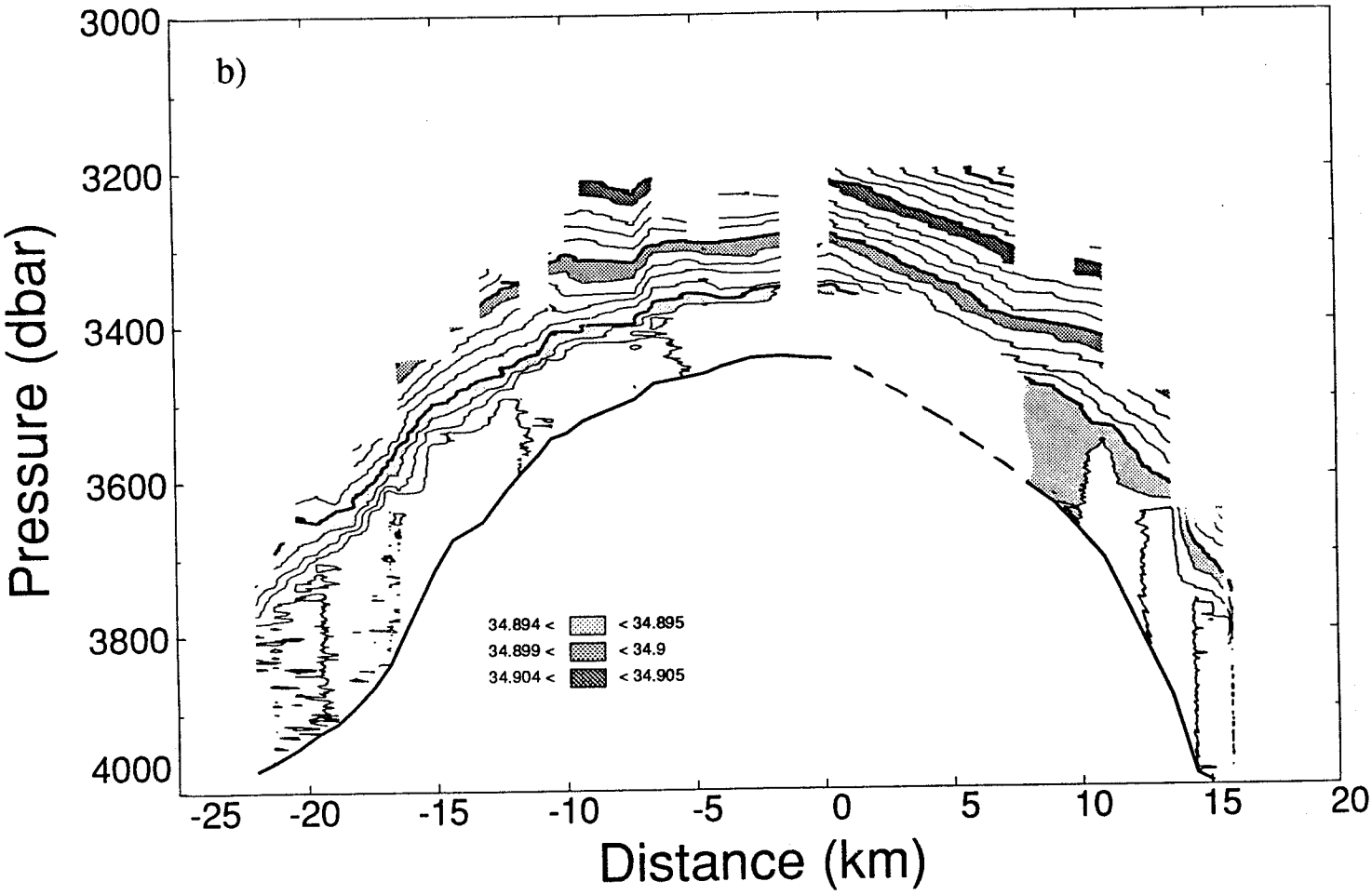

Figure 4.4. (continued) b) Salinity. Contour interval is 0.001 PSU.

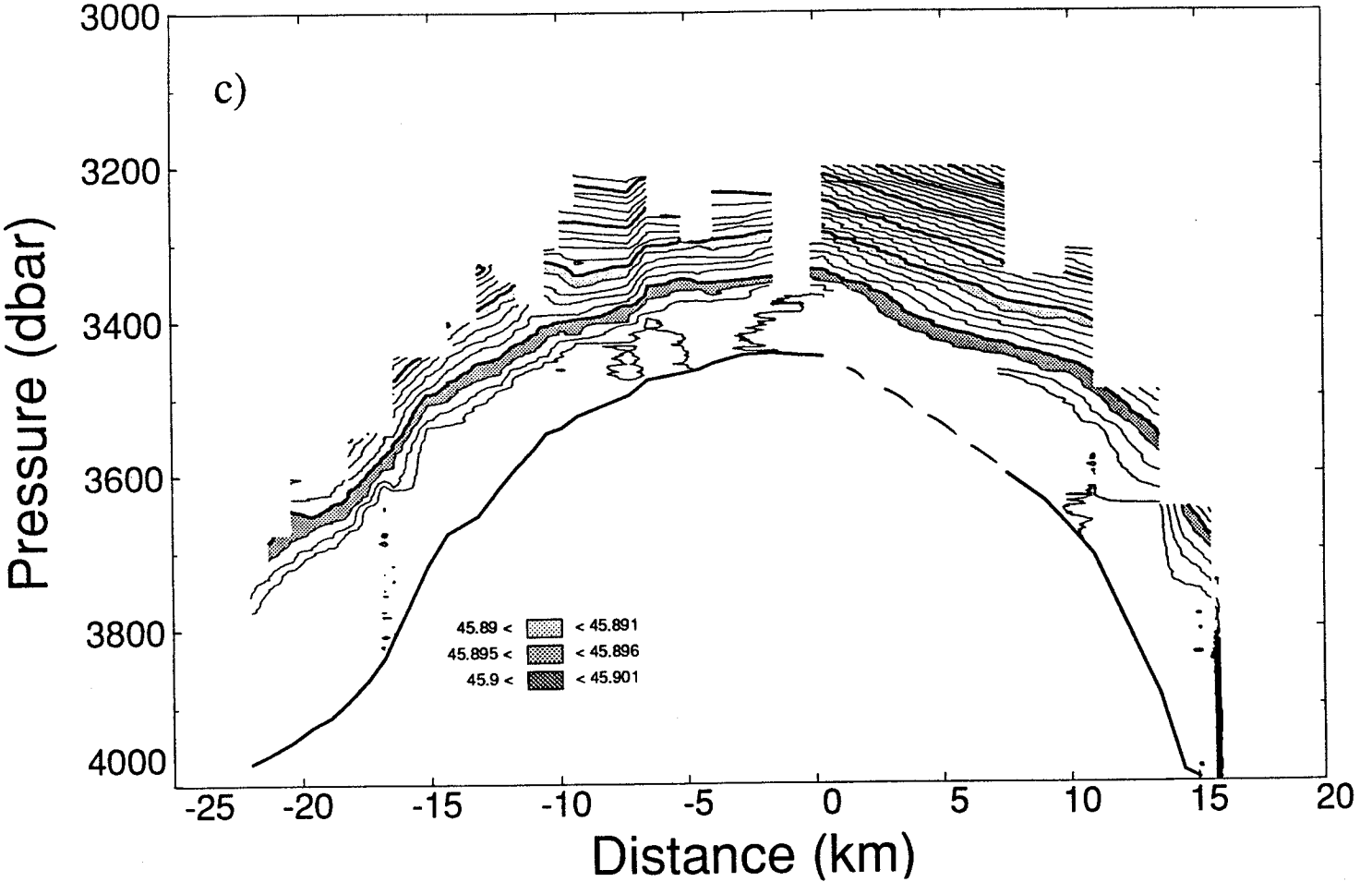

Figure 4.4. (continued) c) Potential density. Contour interval is 0.002 kg m^{-3}.

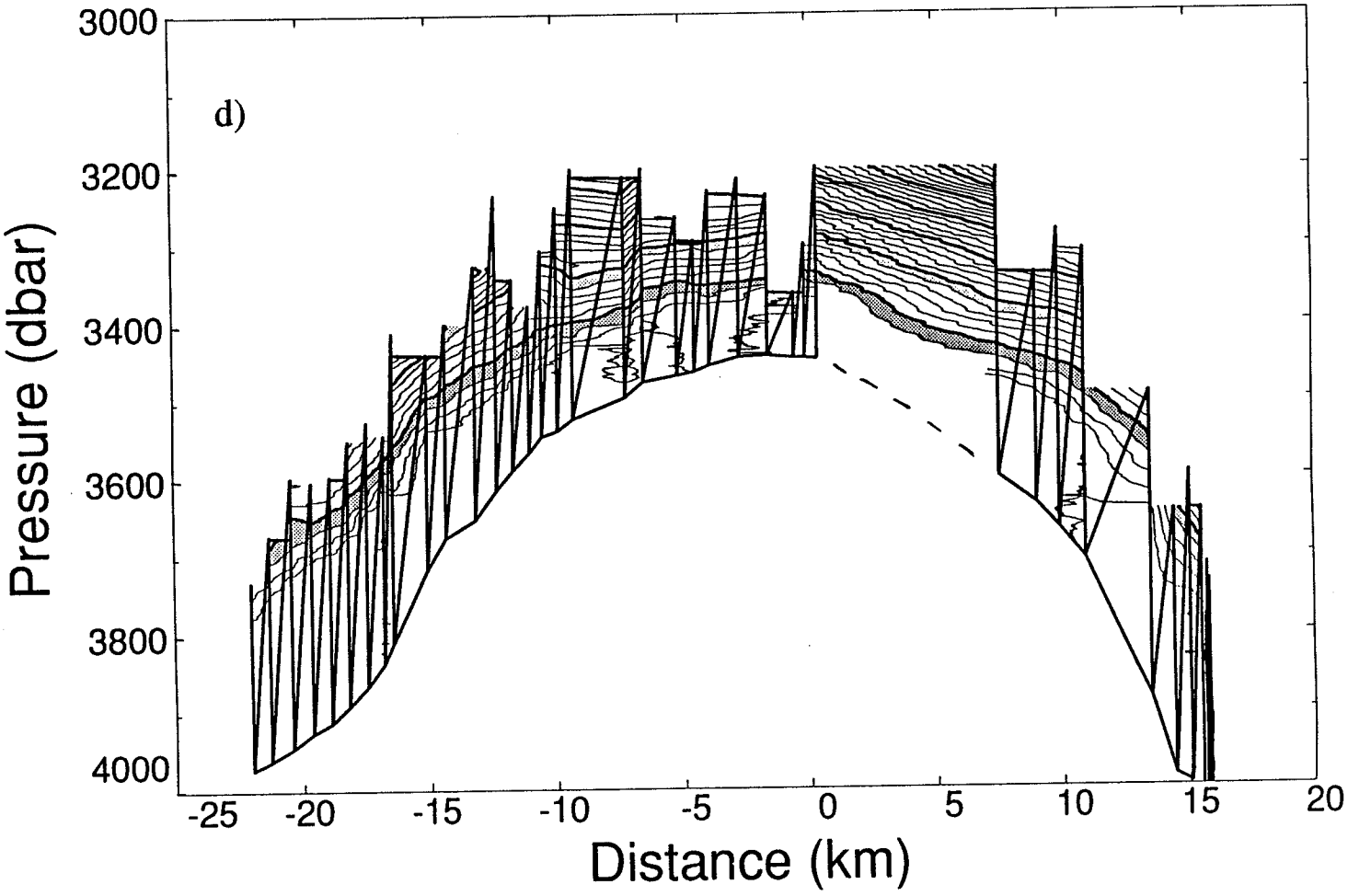

Figure 4.4. (continued) d) Path of the CTD during the two tow-yo's plotted over the potential density contours.

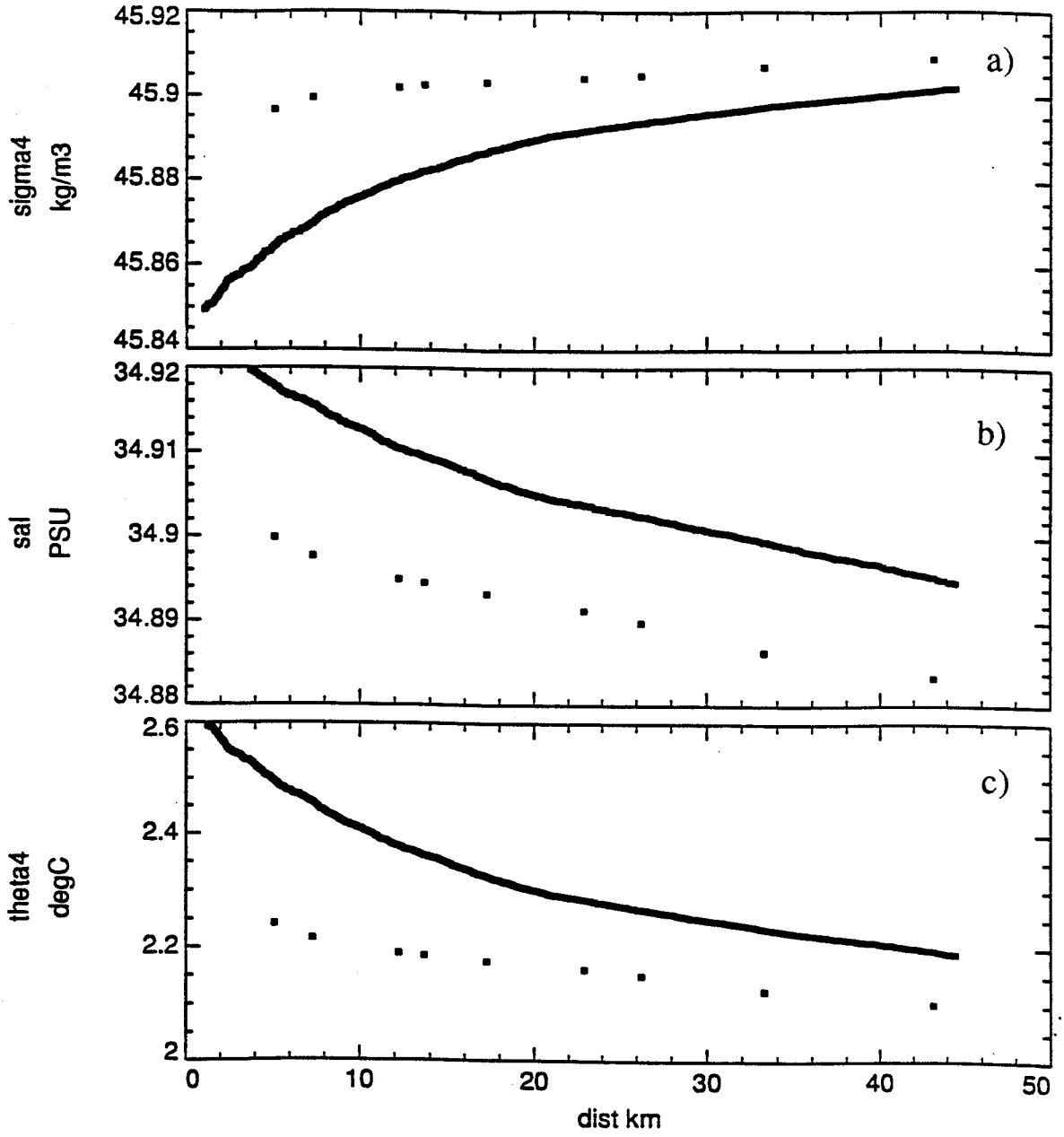

Figure 4.5. a) Potential density, b) salinity and c) potential temperature plotted against distance from the Ridge crest along Section 2. The dots represent data averaged over the bottom 100 m of AVP profiles. The thick lines are the data from an offshore site (AVP drop 463) projected laterally (westward) until the bottom is encountered on the shoaling Ridge.

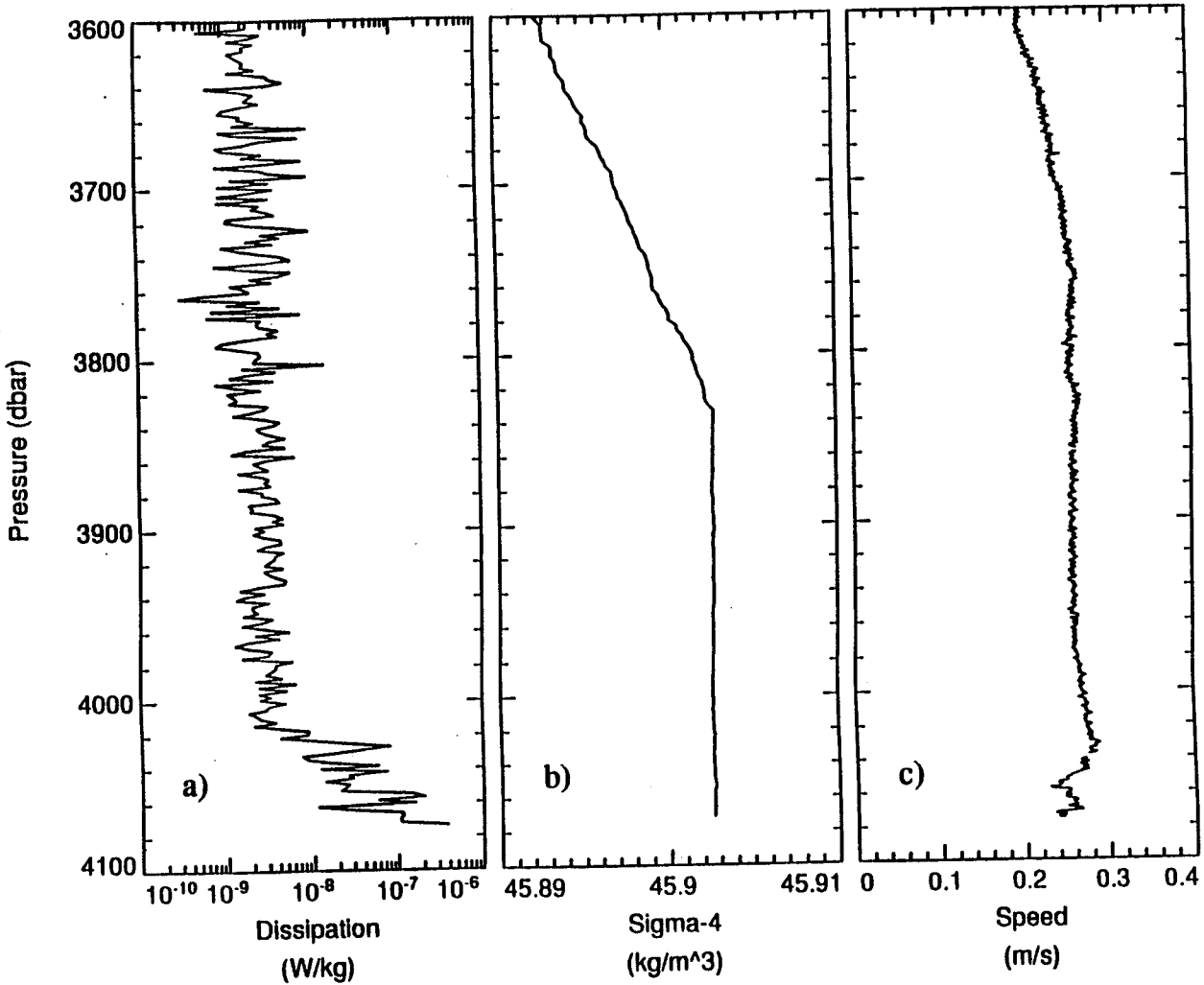

Figure 4.6. Profiles of a) dissipation rate, b) density and c) flow speed from AVP drop 484. Notice the higher dissipation levels within 50 m of the bottom, and the thick, well-mixed bottom boundary layer seen in the density profile.

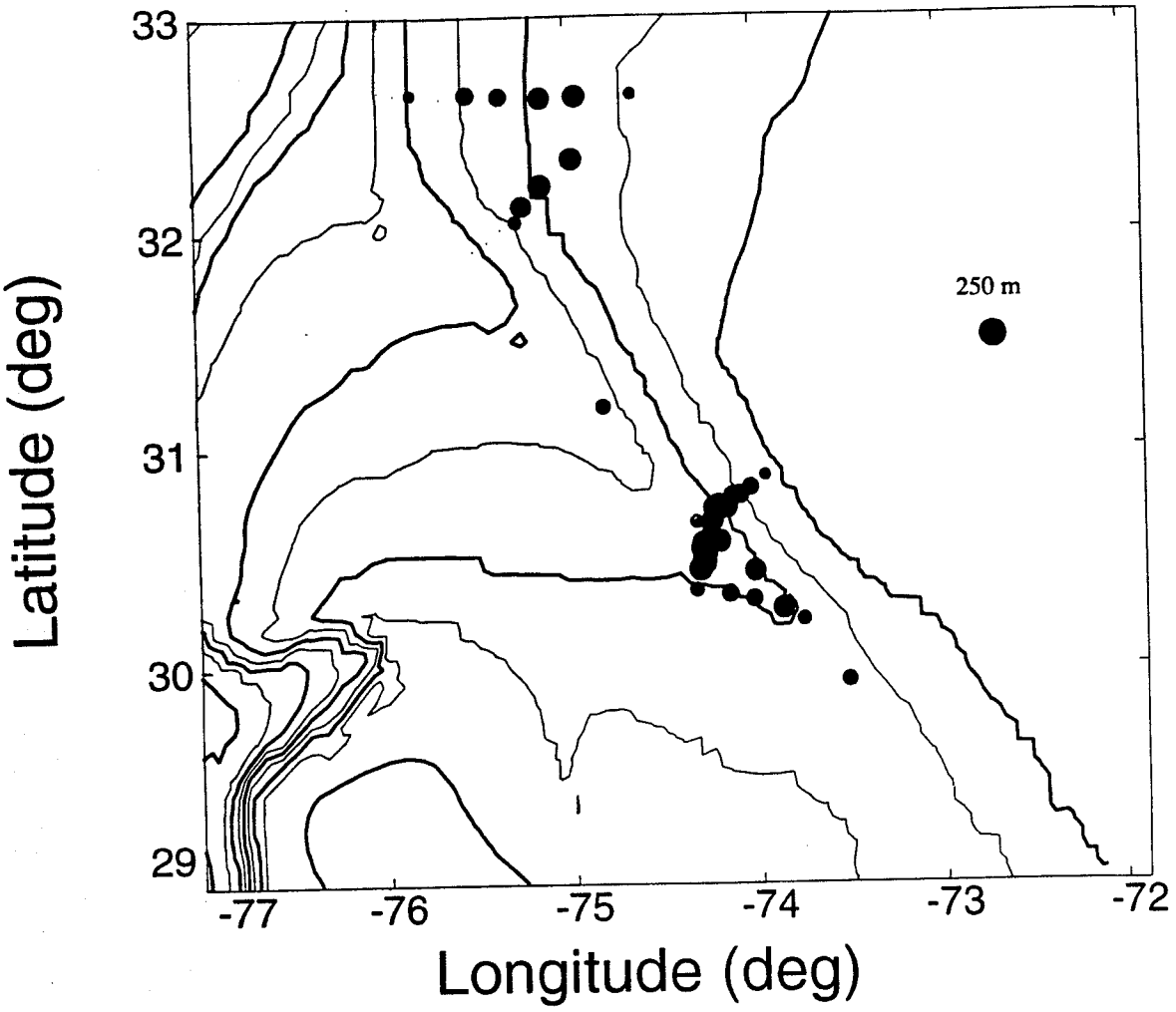

Figure 4.7. Bottom boundary layer (BBL) thicknesses for each AVP drop. The thickest part of the BBL is 270 m thick. The dot labelled 250 m on the right of the plot gives a reference size.

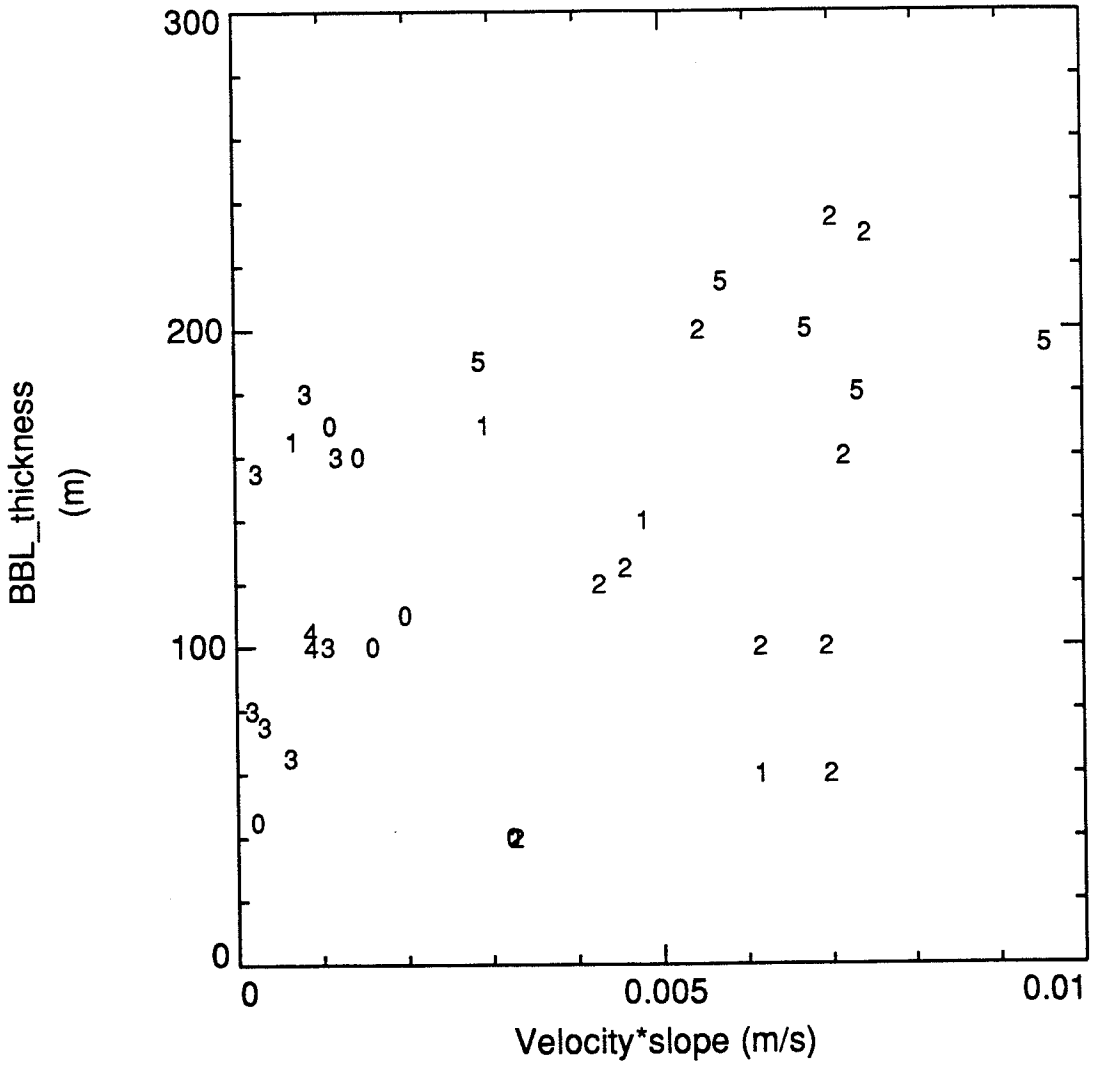

Figure 4.8. Bottom boundary layer (BBL) thickness versus flow speed times bottom slope for each AVP drop. The number plotted is the Section number for the AVP drop.

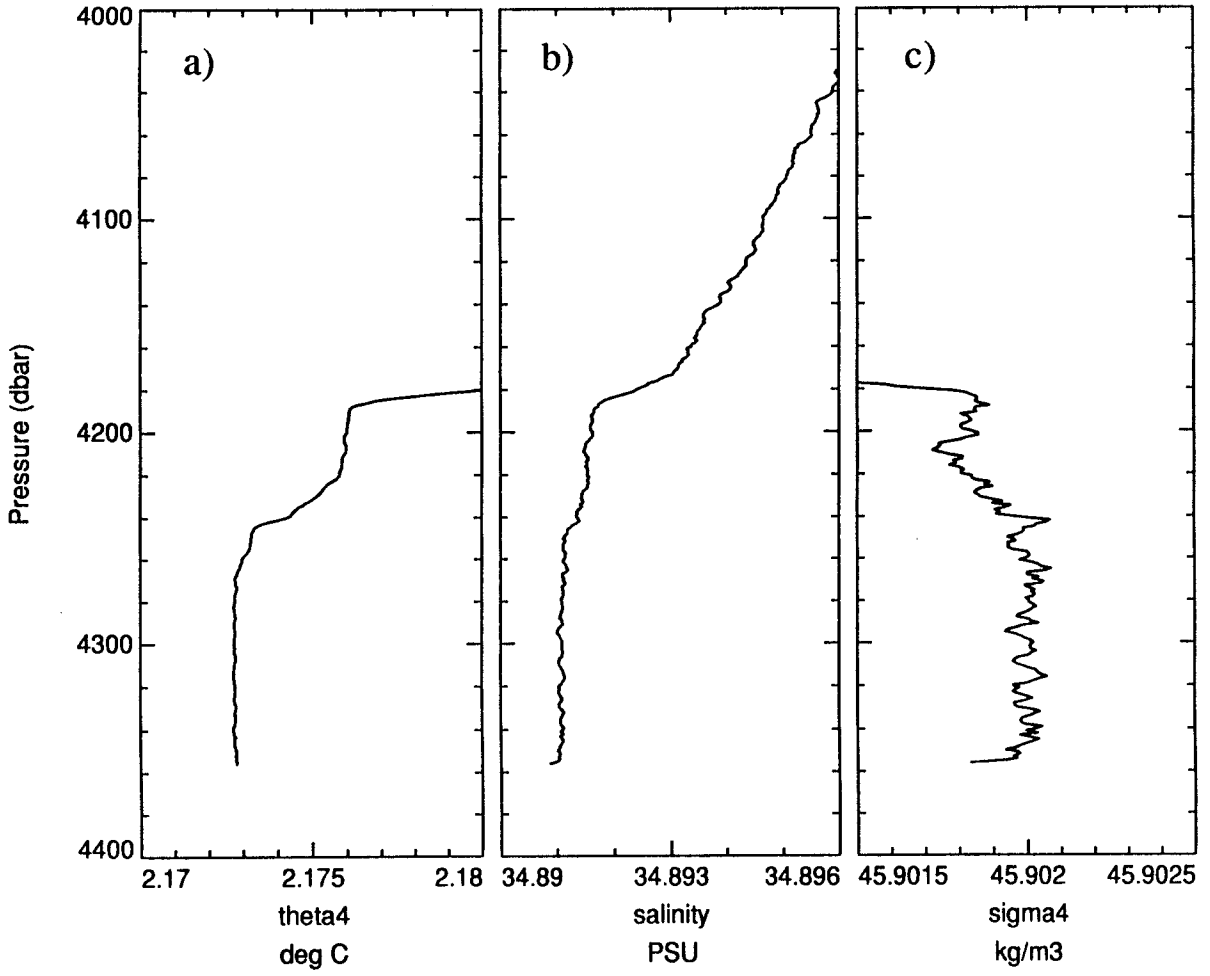

Figure 4.9. An example of a step in the water properties in the bottom boundary layer. Data are from AVP drop 488 and are averaged over 4 dbar bins every 1 dbar. a) Potential temperature. b) Salinity. c) Potential density.

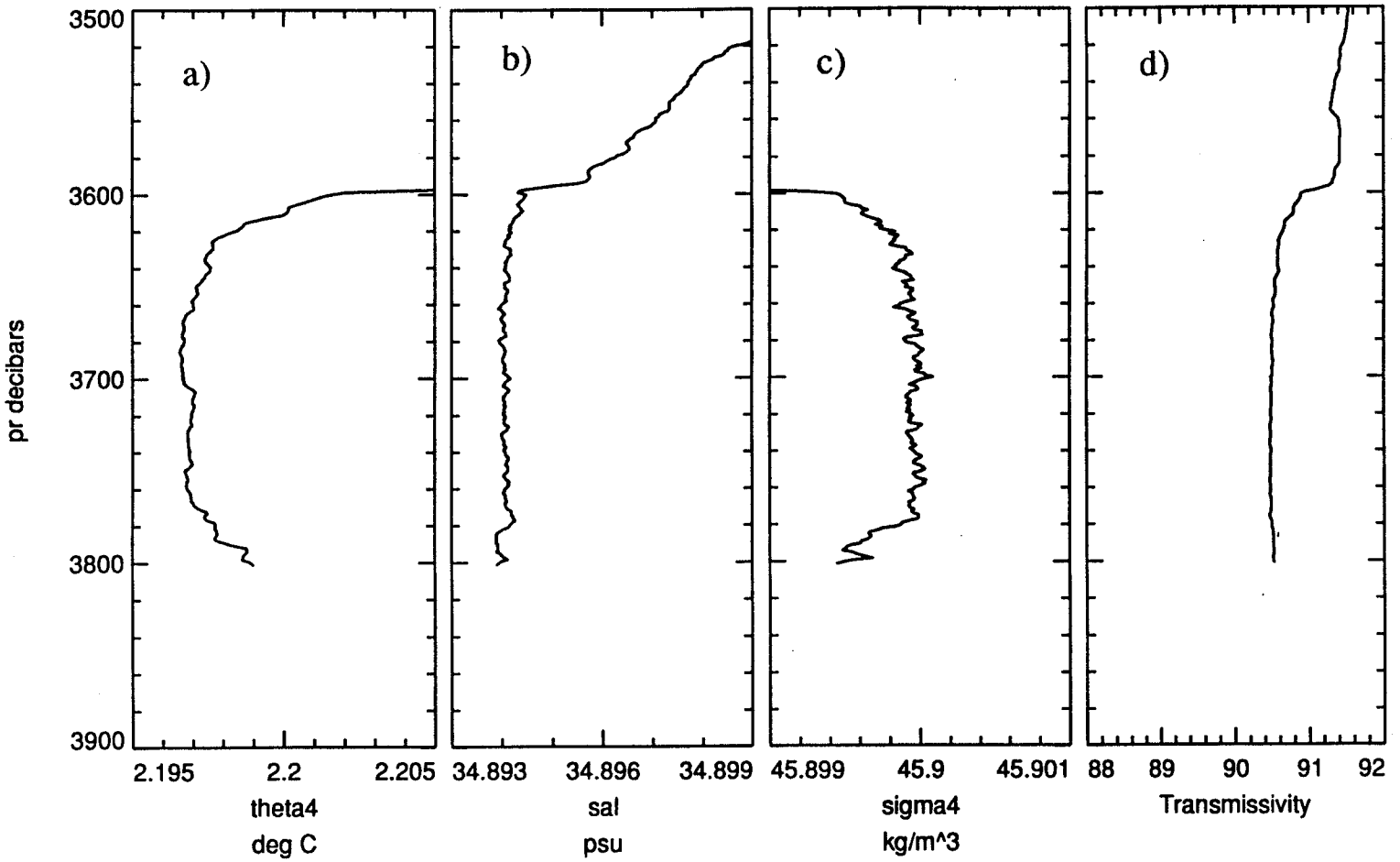

Figure 4.10. Example of a step in the water properties in the bottom boundary layer. Data are from CTD 31 and are averaged over 4 dbar bins every 1 dbar. The water in the bottom 20 m is lighter than the overlying water in the BBL. This less dense layer has a lower salinity than the water above the BBL at the same density. a) Potential temperature. b) Salinity. c) Potential density. d) Transmissivity, in arbitrary units.

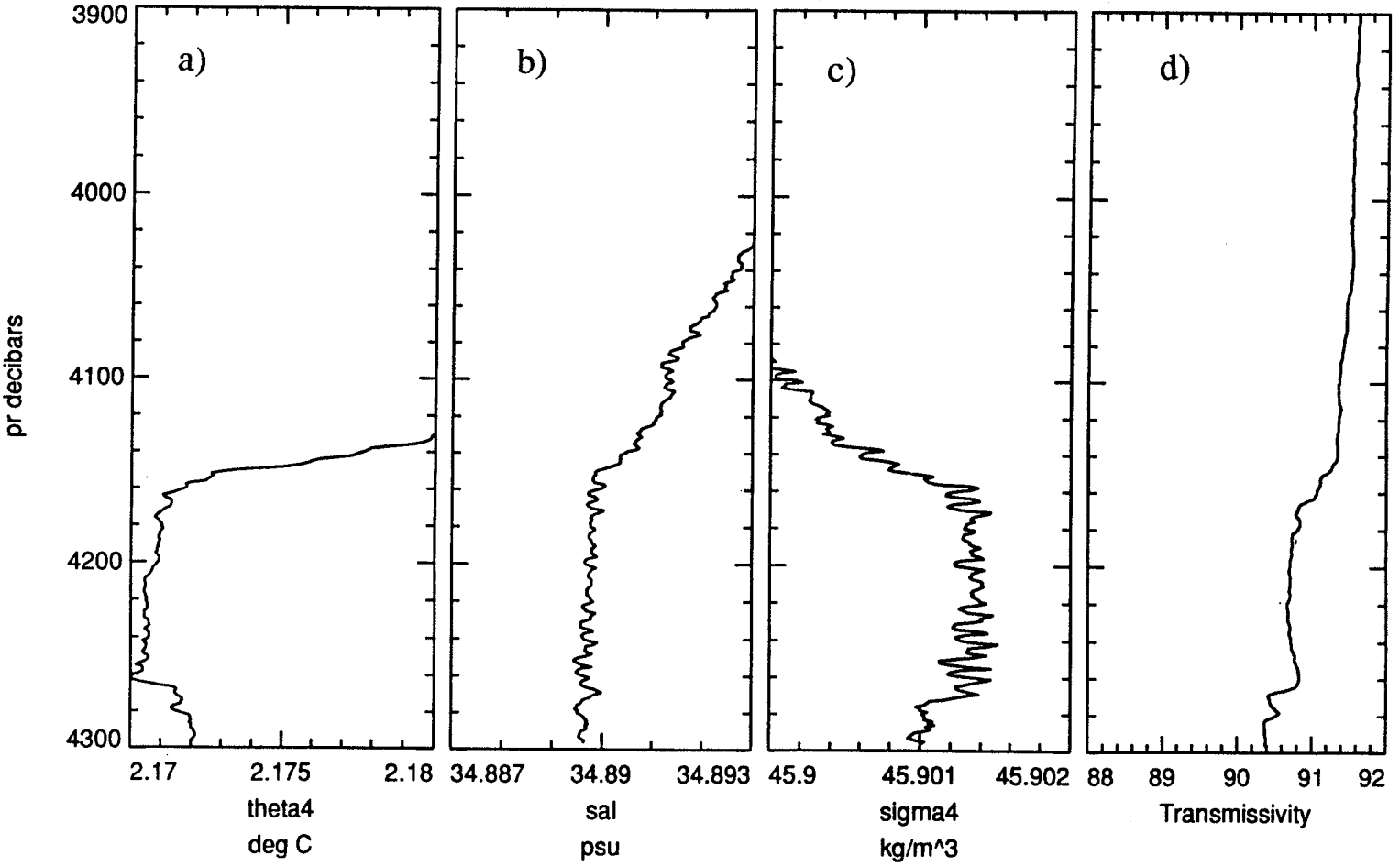

Figure 4.11. Example of a step in the water properties in the bottom boundary layer. Data are from CTD 26 at Site 2-7 and are averaged over 4 dbar bins every 1 dbar. The water in the bottom 35 m is lighter than the overlying water in the BBL. a) Potential temperature. b) Salinity. c) Potential density. d) Transmissivity, in arbitrary units.

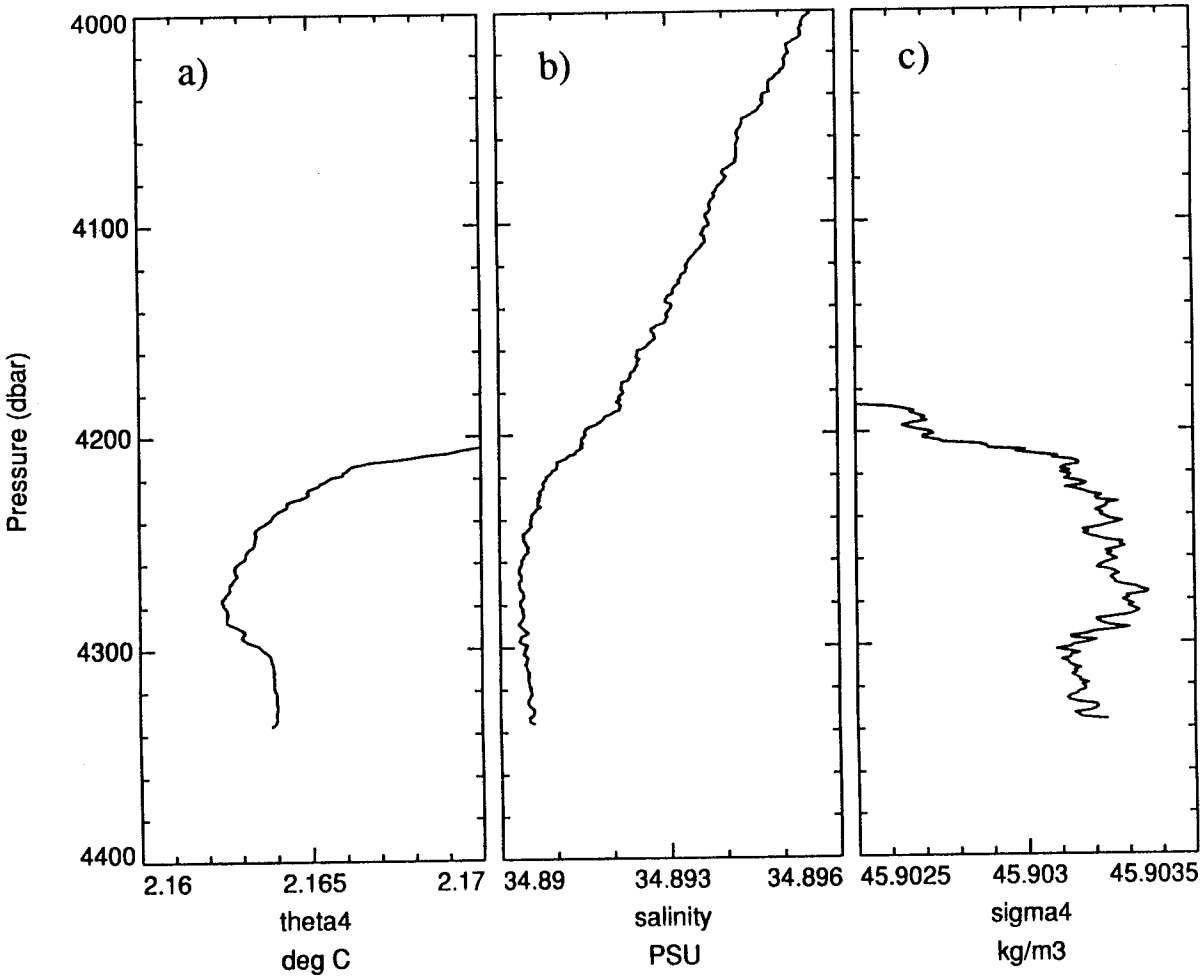

Figure 4.12. Data are from AVP drop 455 at Site 2-7 and are averaged over 4 dbar bins every 1 dbar. This profile is at the same site as CTD 26 shown in Figure 4.10 and shows the same step in temperature in the BBL as the CTD profile in the bottom 35 dbar. a) Potential temperature. b) Salinity. c) Potential density.

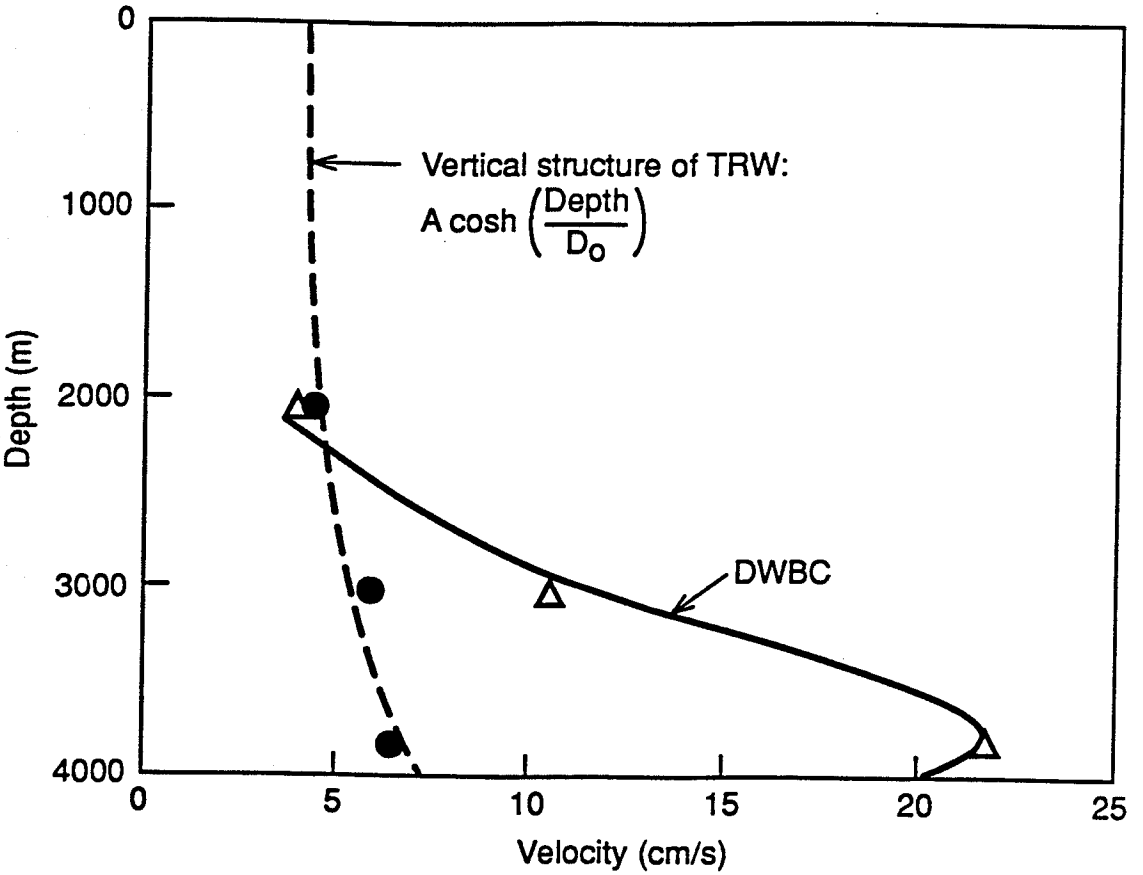

Figure 4.13. Comparison of mean flow (triangles) and time-varying flow (circles) from the current meter mooring on the east flank of the BBOR (Mills and Rhines, 1979). The water depth is 4000 m. The vertical structure of the time-varying flow is consistent with the theoretical structure of a topographic Rossby wave. The solid curve is an estimate of the vertical structure of the DWBC based on the mean flow measurements; the flow structure in the bottom boundary layer below the current meter at 3800 m (the lowest triangle) is unknown.

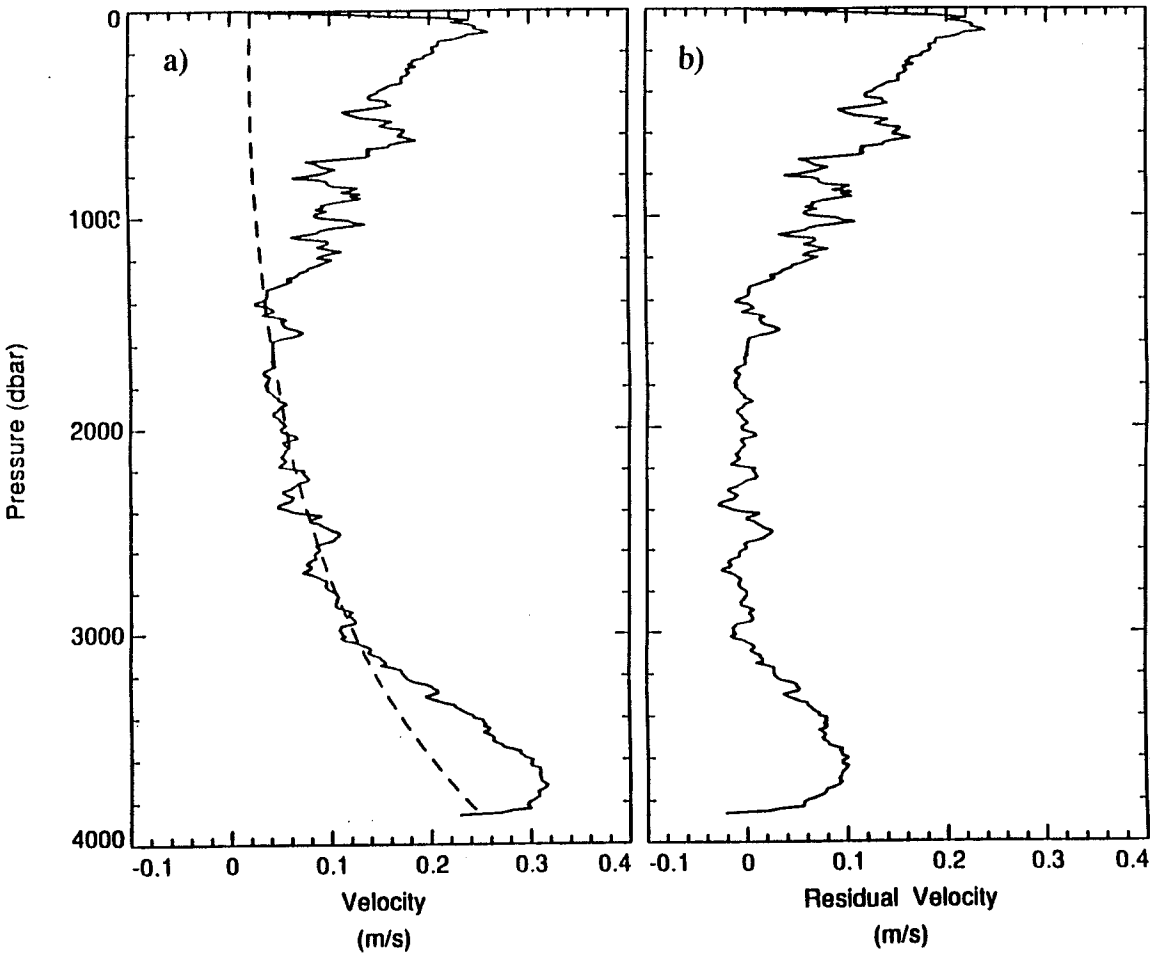

Figure 4.14. Velocity profiles from AVP drop 487 at Site 2-3. a) The observed velocity profile with both DWBC and TRW components. The dotted line represents the hyperbolic cosine fit to the profile between the depths of 1400 and 3000 dbar; this fit represents the TRW component of flow. b) The residual after the TRW component has been removed. We consider this residual flow below 3000 dbar to be the DWBC.

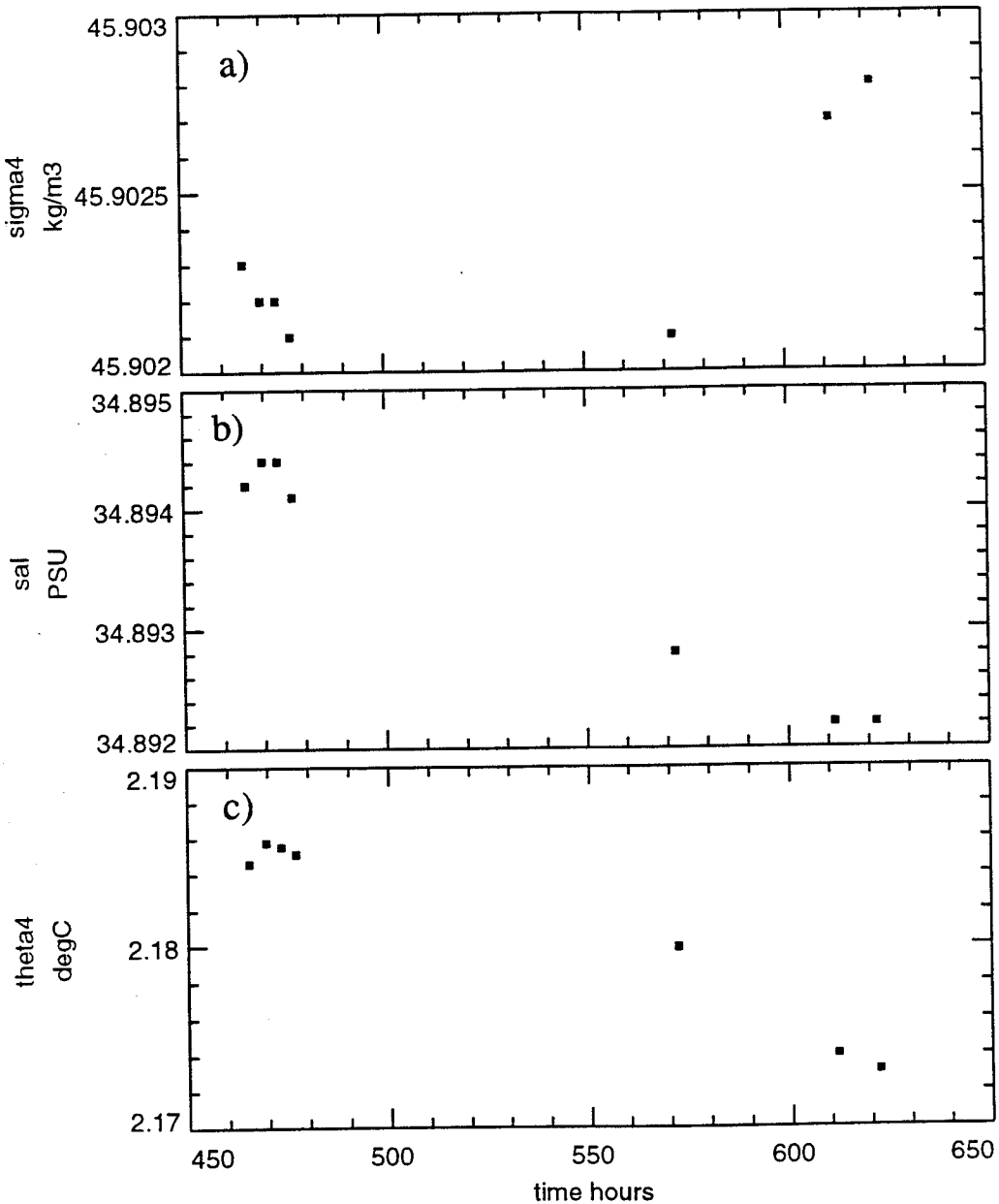

Figure 4.15. Time-series of a) potential density, b) salinity and c) potential temperature at Site 2-5. Data are from AVP drops 464, 465, 467, 469, 484, 489 and 492. Each data point represents an average over the bottom 100 dbar of the profile.

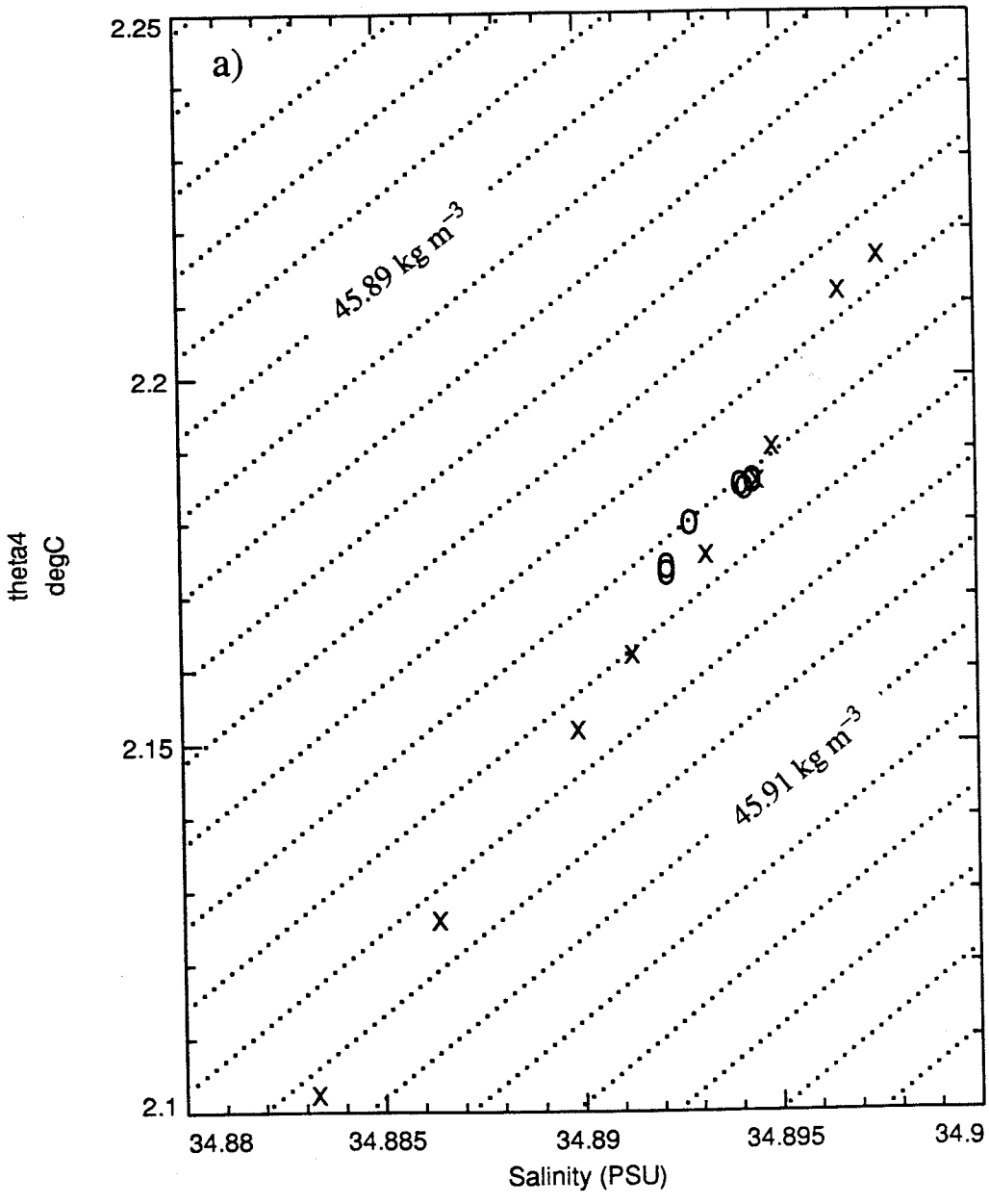

Figure 4.16. a) Potential temperature versus salinity. The letter "x" indicates data from the first survey of Section 2, from July 28, 1992, to July 30, 1992. Open circles are data from the time-series at Site 2-5. Data represent averages over the bottom 100 dbar of AVP profiles. The dotted lines are potential density contours every 0.002 kg m^{-3}

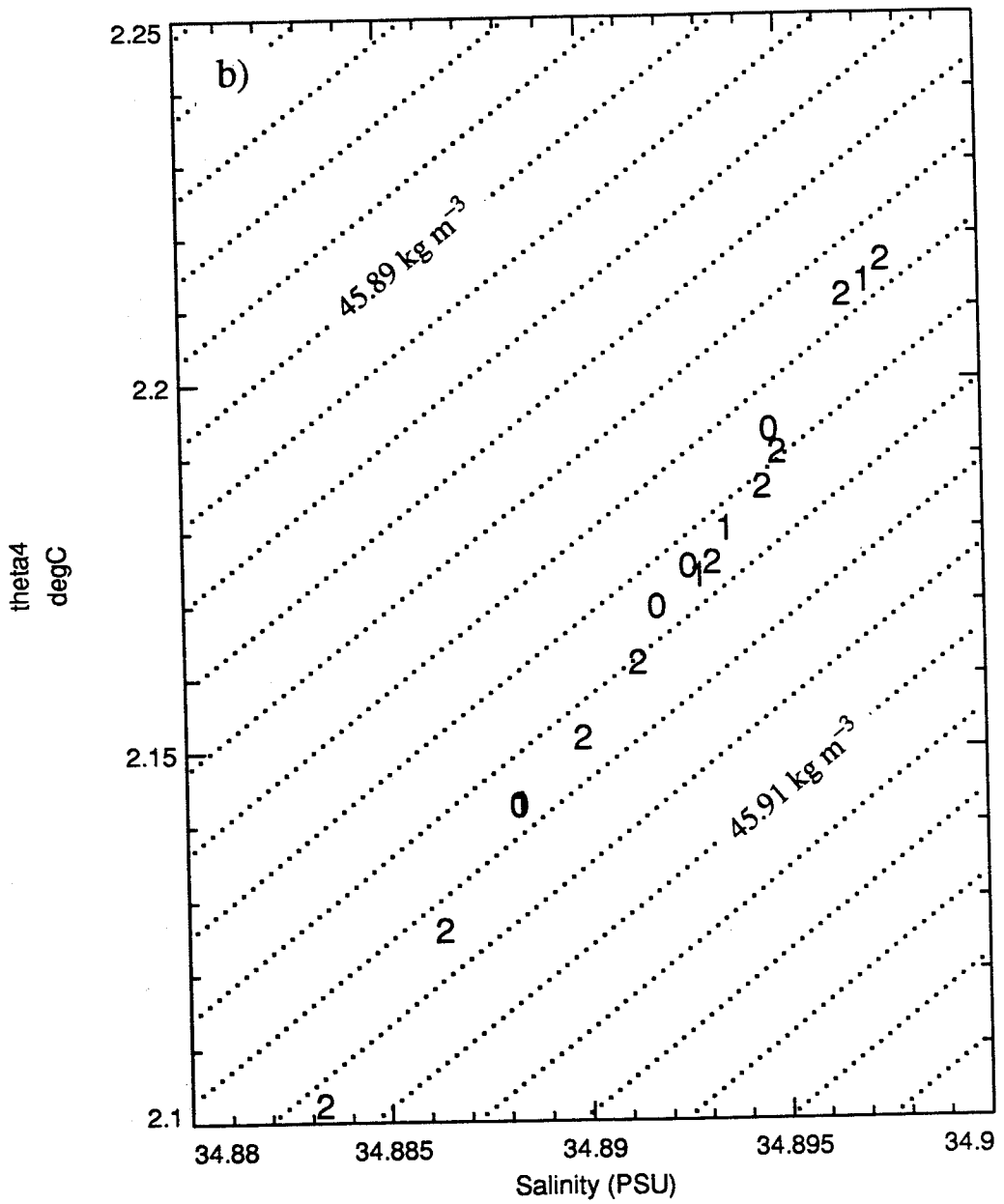

Figure 4.16. (continued) b) Potential temperature versus salinity on Sections 0, 1 and 2. The numbers plotted indicate the numbers of the Section from which the data were taken. Data from Section 2 are from the first survey only, from July 28, 1992, to July 30, 1992. Data represent averages over the bottom 100 dbar of AVP profiles. The dotted lines are potential density contours every 0.002 kg m^{-3}

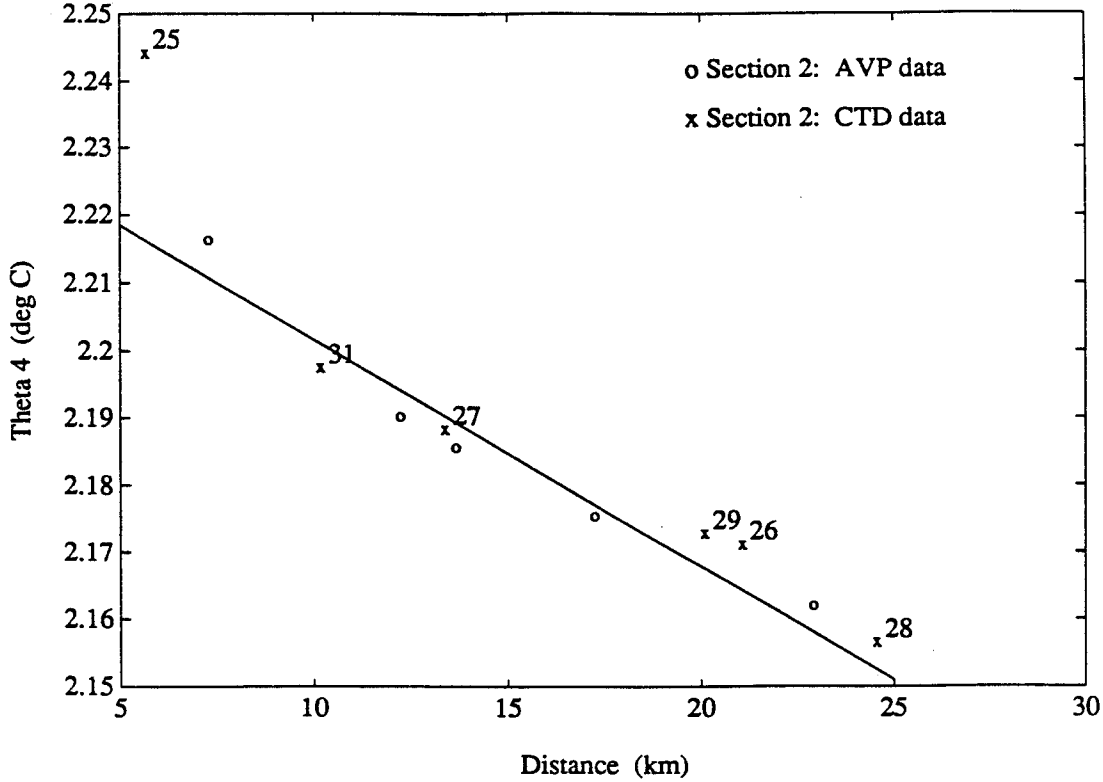

Figure 4.17. Potential temperature versus cross-slope distance on Section 2. Data represent the average temperature over the bottom 100 dbar. The solid line is a least-squares linear fit to the AVP data only. CTD data are shown for comparison and are labeled with the CTD cast number. CTD 27 is near Site 2-5, which was at a distance of 15 km from the Ridge crest.

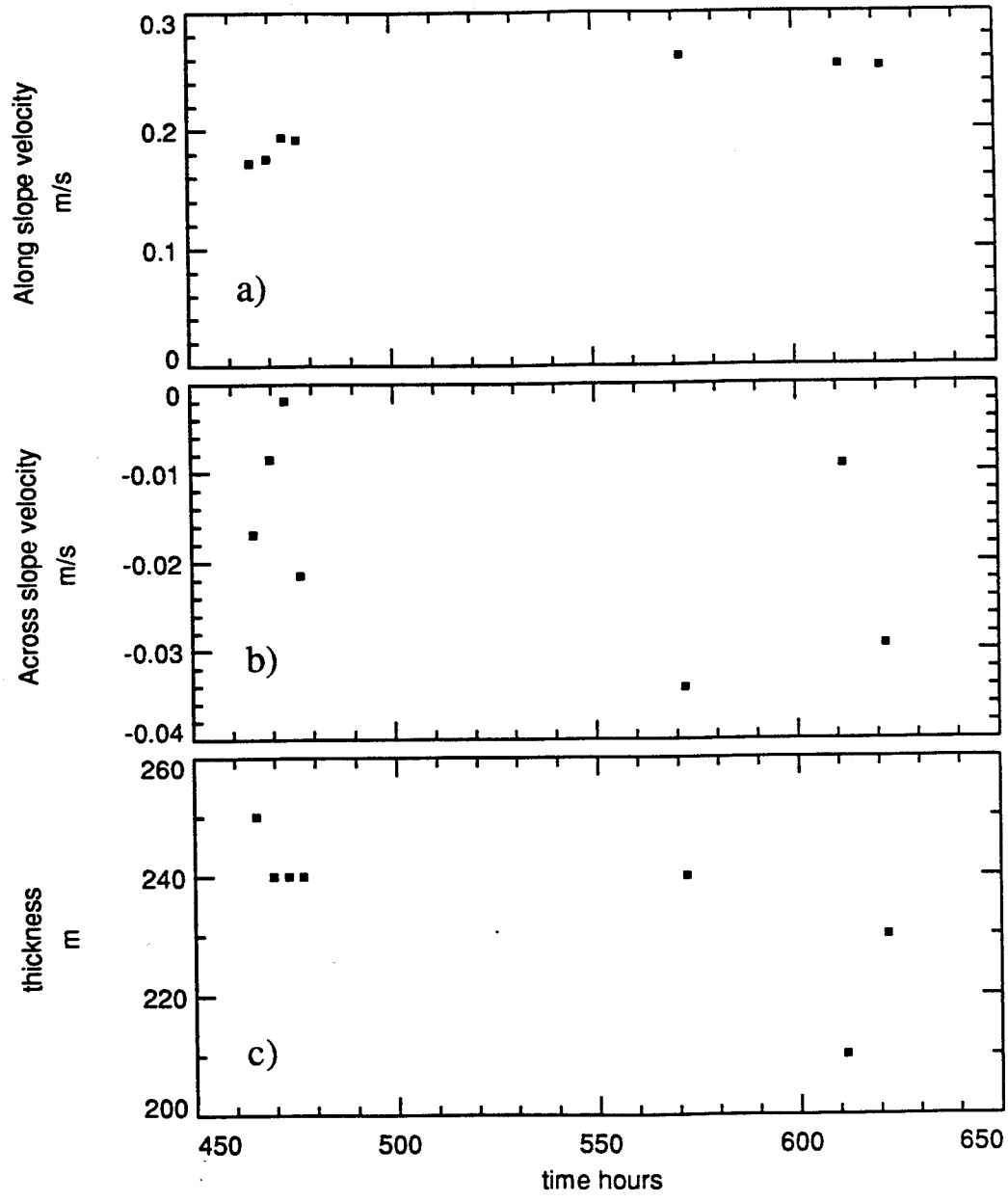

Figure 4.18. Time-series of a) along-slope velocity, b) across-slope velocity and c) bottom boundary layer thickness at Site 2-5. Data represent averages over the bottom 100 dbar. The velocity components are determined by assuming that the down-slope direction of the Ridge was 55° from true north and that the magnetic declination was 7.5° W.

Chapter 5. Summary and Suggestions for Further Analysis

This experiment to study the DWBC was a success. The AVP performed better than the CTD in profiling water properties in the bottom boundary layer (BBL) and the relative velocity profiles were accurate to about 0.14 cm s^{-1}. The absolute velocity profiles were accurate to better than 3 cm s^{-1}, but without further analysis of the data, we can not say how much better. In addition, these simultaneous profiles of velocity and density are unique. These data provide a valuable data set for analysis of the DWBC.

The ability to use the AVP temperature and conductivity sensors on the CTD as secondary sensors proved valuable both for the high quality of data and for identifying the faulty primary temperature sensor on the CTD.

The BBL was remarkably homogeneous in the vertical and horizontal, with the exception of small steps in the vertical profiles of temperature, salinity and density. Some of these observed steps were unstable; we estimated that a typical step would last on the order of 2 hours before overturning. On the other hand, two profiles 3 hours apart at the same location showed similar unstable profiles. The suspended sediment in the CTD cast (Figure 4.11) showed an increase in the lower layer; the density increase due to the sediment increase might have stabilized the density profile. If indeed this was the same feature in the two profiles, the feature's size must have been on the order of 2 km. We could not estimate how quickly turbulence would dissipate these steps since the dissipation rate data were beneath the noise level of the measurement.

In Section 4.1, we pointed out the similarity between the isopycnal tilt and bottom slope at Sections 2 and 5. Since the Ridge was created and maintained by interaction with the DWBC and the sediment that the current carries, an interesting question is whether the similarity of isopycnal tilt and bottom slope here was dynamically constrained or simply fortuitous.

We observed TRW's in the vertical structure of the velocity profiles and in the spatial and temporal structure of the BBL on Section 2. From the potential temperature data at Site 2-5, we inferred an up-slope velocity of 0.6 cm/s in the BBL due to the TRW. The AVP absolute velocity profiles were not accurate enough to observe this

up-slope flow, both because of variability between drops and because of uncertainty in the orientation of the topography.

Questions which remain unanswered by this analysis are:

- What maintains the bottom boundary layer? Does topographic Rossby wave rectification at the Ridge contribute energy to the maintainence of the BBL?
- Can the BBL thickness be parametrized on local properties of the flow? Or does the thickness depend on the history of the flow, such as up-stream gradients or changes in bottom slope?
- What causes the observed steps in profiles of water properties in the BBL?

REFERENCES

Amos, A.F., A.L. Gordon, and E.D. Schneider, 1971: Water masses and circulation patterns in the region of the Blake-Bahama Outer Ridge. *Deep-Sea Res.*, **18,** 145-165.

Brewer, P.G., W.S. Broecker, W.J. Jenkins, P.B. Rhines, C.G. Rooth, J.H. Swift, T. Takahashi, and R.T. Williams, 1983: A Climatic Freshening of the Deep Atlantic North of 50°N over the Past 20 years. *Science,* **222,** 1237-1239.

Drever, R.G., J.H. Dunlap and T.B. Sanford, 1984: The Design and Performance of an Acoustic Doppler and Electromagnetic Velocity Profiler. APL-UW 9-84, Applied Physics Laboratory, University of Washington, Seattle, WA.

Fine, R.A. and R.L. Molinari, 1988: A continuous deep western boundary current between Abaco (26.5 °N) and Barbados (13°N). *Deep-Sea Res.*, **35,** 1441-1450.

Fofonoff, N.P., 1981: The Gulf Stream System. *In: Evolution of Physical Oceanography,* B. Warren and C. Wunsch (Eds.), MIT Press, Cambridge, MA., 620pp.

Garrett, C., 1990: The role of secondary circulation in boundary mixing. *J. Geophys. Res.*, **95,** 3181-3188.

Garrett, C., P. MacCready, and P. Rhines, 1993: Boundary mixing and arrested Ekman layers: Rotating stratified flow near a sloping boundary. *Annu. Rev. Fluid Mech.*, **25,** 291-323.

Gregg, M.C., 1987: Diapycnal Mixing in the Thermocline: A Review. *J. Geophys. Res.*, **92,** 5249-5286.

Hogg, N.G. and H. Stommel, 1985: On the relation between the deep circulation and the Gulf Stream. *Deep-Sea Res.*, **32,** 1181-1193.

Jenkins, W.J. and P.B. Rhines, 1980: Tritium in the deep North Atlantic Ocean. *Nature,* **286,** 877-880.

Lai, D.Y., 1984: Mean Flow and Variabilities in the Deep Western Boundary Current. *J. Phys. Oceanogr.*, **14,** 1488-1498.

Larsen, J.C. and T.B. Sanford, 1985: Florida Current volume transports from voltage measurements. *Science,* **227,** 302-304.

Lazier, J.R.N., 1988: Temperature and salinity changes in the deep Labrador Sea, 1962-1986. *Deep-Sea Res.*, **35,** 1247-53.

Leaman, K.D., 1989: Relationship of Gulf Stream meandering to the strength of the Deep Western Boundary Current. *Eos, Trans. Amer. Geophys. Union,* **70,** p. 364.

Leaman, K.D. and J.E. Harris, 1990: A note on the average absolute transport of the Deep Western Boundary Current east of Abaco Island, the Bahamas. *J. Phys. Oceanogr.*, **20,** 467-475.

Lee, T.N., W. Johns, F. Schott, and R. Zantopp, 1990: Western Boundary Current Structure and Variability East of Abaco, Bahamas at 26.5°N. *J. Phys. Oceanogr.*, **20,** 446-466.

MacCready, P.M. and P.B. Rhines, 1991: Buoyant inhibition of Ekman transport on a slope and its effect on stratified spin-up. *J. Fluid Mech.*, **223,** pp. 631-661.

Mills, C.A., and P.B. Rhines, 1979: The deep western boundary current at the Blake-Bahamas outer ridge: Current meter and temperature observations, 1977-1978. WHOI Tech. Rep. 79-85, 77 pp.

Munk, W.H., 1966: Abyssal recipes. *Deep-Sea Res.*, **13,** 707-730.

Olson, D.B., G. Ostlund, and J. Sarmiento, 1986: The Western Boundary undercurrent off the Bahamas. *J. Phys. Oceanogr.*, **16,** 233-240.

Pickart, R., N. Hogg, and W. Smethie, 1989: Determining the strength of the deep western boundary current using the chlorofluoromethane ratio. *J. Phys. Oceanogr.*, **19,** 940-951.

Pickart, R. and D.R. Watts, 1990: Deep Western Boundary Current variability at Cape Hatteras. *J. Mar. Res.*, **48,** 765-791.

Rhines, P., 1970: Edge-, bottom-, and Rossby waves in a rotating stratified fluid. *Geophys. Fluid Dyn.*, **1,** 273-302.

Richardson, P.L., 1977: On the crossover between the Gulf Stream and the Western Boundary Undercurrent. *Deep-Sea Res.*, **24,** 139-159.

Riser, S.C., H. Freeland, and H.T. Rossby, 1978: Mesoscale motions near the western boundary of the North Atlantic. *Deep-Sea Res.*, **25,** 1179-1191.

Roemmich, D. and C. Wunsch, 1984: Apparent changes in the climate state of the deep North Atlantic Ocean. *Nature,* **307,** 447-450.

Sanford, T.B., R.G. Drever and J.H. Dunlap, 1985: An acoustic Doppler and electromagnetic velocity profiler. *J. Atmos. Ocean. Tech.*, **2,** 110-124.

Smethie, W.M.Jr., and S. Trumbore, 1984: Chlorofluoromethanes (F-11 and F-12) in the western North Atlantic Ocean and the deep western boundary undercurrent. *Eos, Trans. Amer. Geophys. Union,* **64,** p. 1089.

Stommel, H.M., 1958: The abyssal circulation. *Deep-Sea Res.*, **5,** 80-82.

Swallow, J.C., and L.V. Worthington, 1961: An observation of a deep counter-current in the western North Atlantic. *Deep-Sea Res.*, **8,** 1-19.

Swift, J.H., K. Aagaard, and S.-A. Malmberg, 1980: The contribution of the Denmark Strait overflow to the deep North Atlantic. *Deep-Sea Res.*, **27A,** 29-42.

Thompson, J.D., and W.J. Schmitz, 1989: A limited-area model of the Gulf Stream: Design, initial experiments and model-data intercomparison. *J. Phys. Oceanogr.*, **19,** 791-814.

Trowbridge, J.H. and S.J. Lentz, 1991: Asymmetric behavior of an Oceanic Boundary Layer above a Sloping Bottom. *J. Phys. Oceanogr.* (submitted).

Weiss, R., L. Bullister, R.H. Gammon, and M.J. Warner, 1985: Atmospheric chlorofluoromethanes in the deep equatorial Atlantic. *Nature,* **314,** 608-610.